The Pennsylvania State University

The Graduate School

Department of Materials Science and Engineering

SYNTHESIS OF PARTICULATES FOR FUNCTIONAL APPLICATIONS: EXAMPLES OF NANOCOMPOSITES AND HEMATITE

A Thesis in

Materials Science and Engineering

by

Jun Wang

Submitted in Partial Fulfillment
of the Requirements
for the Degree of

Doctor of Philosophy

August 2004

The thesis of Jun Wang was reviewed and approved* by the following:

James H. Adair
Professor of Materials Science and Engineering
Thesis Co-Advisor
Co-Chair of Committee

William B. White
Professor Emeritus of Geochemistry
Thesis Co-Advisor
Co-Chair of Committee

Thomas E. Mallouk
Dupont Professor of Materials Chemistry

Erwin A. Vogler
Associate Professor of Materials Science and Engineering

Gary L. Messing
Distinguished Professor of Ceramic Science and Engineering
Head of the Department of Materials Science and Engineering

*Signatures are on file in the Graduate School

ABSTRACT

The size and shape dependence of optical properties for particulate materials were investigated in this thesis research. Specific materials of interests include α-Fe_2O_3 pigments, Ag/SiO_2 core-shell structured nanocomposites and tabular SiO_2 nanoparticles. The main focus was on the processing parameters related to the particulate morphologies, dispersion and optical properties of each model system and optimization of those conditions so that a general prediction for the optical behavior of the particulate materials was achievable.

Iron oxide (hematite) particles with various shapes (platelet, polyhedron, pseudocube and peanut-like) were synthesized by hydrothermal treatment of a $Fe(OH)_xO_y$ precursor under various conditions. The size and shape of hematite particles could be adjusted by carefully controlling the processing parameters such as holding time, temperature and adsorption ions present in the system. The nearly monosized α-Fe_2O_3 platelets possessed face diameters of approximately 3 μm and a thickness of 0.5 μm under scanning electron microscope (SEM). The apparent color of the particles changed as particle size and shape varied. Munsell color notation was employed to compare the color of hematite particles with various size and shape. Diffuse reflectance spectra showed that a "red-shift" of 40 nm was observed in platelet, pseudocube and peanut-like particles compared to conventional particles. The band at 850 nm for the $^6A_1 \rightarrow {}^4T_1$ transition was split in the pseudocubic and peanut-like particles. Raman spectra of the hematite particles also revealed that the vibrational modes of α-Fe_2O_3 particles diminished as particle size decreased, and dependence of vibrational band intensity to

frequency was also observed. The spectral profiles demonstrated significant difference as excitation lines changes from blue (457 nm) to red (647 nm). Unexpectedly, a weak near-infrared luminescence was observed for fine-particle α-Fe_2O_3 when excited by 1064 nm radiation from a Nd-YAG laser. There were three broad luminescence peaks at 7994, 7225 and 6686 cm^{-1}, with intensities about ten times that of the Raman scattering. The relative intensities varied with particle morphology and with heat treatment. Overall band intensities increased by about a factor of ten for Fe_2O_3 that has been heated to 500 °C and then decreased again for material that has been heated to 1000 °C. The emission was assigned to the $^4T_{1g} \rightarrow {}^6A_{1g}$ crystal field transition of octahedral Fe^{3+}. A large Stokes shift is associated with these transitions. Possible mechanisms responsible for the optical properties of hematite particles were postulated based on the findings of the experiments.

Nanoscale Ag/SiO_2 composite particles with a uniform core-shell structure were synthesized by reverse micelle techniques. The silver cluster was about 5 nm and the silica shell thickness was 10 nm when R=2 (R=[water]/[surfactant]), H=100 (H=[water]/[TEOS]) and X=1 (X= $[NH_4OH]$/[TEOS]) was employed for the cyclohexane/Igepal/water tertiary system. A model calculation indicated that the optical properties of the nanocomposites, especially the refractive index for core-shell structured nanoparticles were governed by the ratio of the core to the shell. The spherical nanocomposite particles were washed and concentrated with high performance liquid chromatography (HPLC) in order to remove the surfactant added during synthesis. Spherical SiO_2 submicron particles were packed in the HPLC column as a stationary phase for the washing and dispersing of Ag/SiO_2 nanocomposite particles. Surface modification of Ag/SiO_2 nanocomposite particles with the silane coupling agent 3-

aminopropyltriethoxysilane (APS) enhanced the charge of the nanoparticles and improved the efficiency of washing with HPLC. Well-dispersed Ag/SiO_2 stable suspensions were successfully attained with ethanol water mixed solvent after HPLC washing based on dynamic light scattering (DLS), transmission electron microscope (TEM) and spin coat/atomic force microscope (AFM) analysis. As a comparison, other conventional methods such as centrifugation, soxhlet extraction and sedimentation were tested and failed to produce well-dispersed Ag/SiO_2 nanocomposite suspensions. The states of the Ag/SiO_2 dispersion were assessed with pH control and average agglomeration number (AAN) analysis. The hypothesis of nanoscale dispersion was evaluated through the washing of Ag/SiO_2 nanocomposite particles with HPLC.

Amorphous tabular SiO_2 nanoparticles were synthesized from the self-assembled octylamine/water bilayer via a template-directed growth mechanism. Morphology of the tabular SiO_2 nanoparticles was analyzed by high-resolution TEM both for room temperature dried and calcined powders. The tabular SiO_2 nanoparticles demonstrated well-defined thickness (4~6 nm) with a relative spread face diameter (100~300 nm), which lead to a wide distribution of aspect ratio based on AFM. High surface area up to 1158 m^2/g was readily obtained with a very uniform micropore size of about 0.63 nm after thermal treatment at 700°C for 2 hours. Metallic Pd clusters were embedded into the microporous SiO_2 matrix via a solution reduction of $Pd(NO_3)_2$ by hydrazine hydrate. The infiltration of 33 wt% Pd leads to a 13 % porosity loss of tabular SiO_2 nanoparticles. The presence of Pd in the pores was demonstrated by energy dispersive X-ray spectroscopy (EDS) and X-ray diffraction (XRD). The metallic guest species presumably resided in the

accessible micropores with an estimated size about 1.3 nm. Hydrogen uptake measurements were performed for the Pd infiltrated nanocomposites.

TABLE OF CONTENTS

LIST OF FIGURES

LIST OF TABLES

ACKNOWLEDGEMENTS

I would like to acknowledge Professors William B. White and James H. Adair for their guidance and patience throughout the course of this work. With their instruction and assistance, I have matured and grown both personally and professionally. They have taught me a great deal through their words and by their example. My sincere gratitude is extended to the members of the doctoral committee, Professor Thomas E. Mallouk and Professor Erwin A. Vogler for their valuable comments.

The Adair and Messing research group members both past and present are greatly acknowledged for their help and generous support during the course of this research work. Special thanks go to Drs. Gugang Chen and Peter Eklund for their assistance with Raman spectra, Dr. Jeffery Kenvin at Micromeritics and Mr. Andrew Smedley at Estee Lauder for their assistance with sample analysis. It is necessary to point out the excellent research environment in MRI and the Department of Materials Science and Engineering that make my accomplishment possible.

The financial support of the NSF Particulate Materials Center at the Pennsylvania State University is gratefully acknowledged. A portion of this work was funded by the Estee Lauder Corporation through the NSF Particulate Materials Center.

Last, but not least, I am gratefully indebted to my parents, my family and my wife Wenyun Yang for their unconditional support and encouragement over many years of education, without which I would have never made it to this point.

Chapter 1

Objectives of Research

The objectives of this research are the understanding of optical properties of particulate materials as a function of particle size and shape, thereby theoretically predicting the macroscopic optical responses of nano to micron scale particulates. The primary materials of interest are ferric oxide (hematite), metal/silica nanocomposites and silica because of their tunable morphologies and excellent optical activities. The accomplishment of the objectives requires controllable and reproducible synthesis and dispersion of particulate materials. The size and shape dependence of optical properties for particles has been noticed but not so well elaborated, and the challenges are to obtain atomic scale correlations of optically active stable nanodispersion and anisotropic particles. Further details on the advancement of this subject will be comprehensively and thoroughly addressed in the following literature review (Chapter 2). Hence, the chapters of this thesis are organized so that the experimental section of this thesis starts out with preparation of anisotropic hematite particles and Ag/SiO_2 nanodispersion. The goal of this research is achieved by creatively conducting critical experiments and systematically analyzing data. A summary of each of the experimental chapters is therefore outlined below:

Chapter 3 Synthesis and Optical Properties of Hematite Particles

- Determine the synthetic parameters that affect the morphology of hematite particles prepared by hydrothermal reaction.
- Evaluate optical properties of hematite particulates with respect to crystal size and shape via spectroscopic analysis.
- Provide guidelines for the prediction of optical properties of pigments based on their crystal structure, size and geometrical shape.

Chapter 4 Synthesis and Optical Properties of Ag/SiO_2 Nanocomposites

- Comparison of agglomeration state of Ag/SiO_2 nanocomposites suspensions using various washing protocols.
- Determine the microscopic mechanisms that induce the agglomeration in nanoparticle dispersions.
- Elaborate the quantum confinement effect of nanocomposite particles through spectroscopic analysis.
- Develop a theoretical approach to estimate the refractive index of nanocomposite particles.

Chapter 5 Dispersion of Silica-Based Nanocomposites with High Performance Liquid Chromatography (HPLC)

- Develop a dispersion scheme to wash and concentrate silica-based nanoscale particles with appropriate modification of particle surfaces.

- Determine the state of dispersion for nanocomposite suspensions so as to understand the mechanisms and generate reproducible products.
- Evaluation of parameters that are pertinent to well-dispersed nanoparticle suspension using HPLC.

Chapter 6 Synthesis and Infiltration of Tabular SiO_2 Nanoparticles

- Manipulate the thickness of anisotropic nanoparticles using self-assembly bilayer systems.
- Determine the growth mechanisms for tabular nanoparticles.
- Perform preliminary studies on porosity of anisotropic particulate materials synthesized by the self-assembly route.
- Find a scheme to infiltrate the microporous anisotropic particulate matrices such that unique properties might be demonstrated.

Chapter 2

Background

2.1 Introduction

The synthesis of anisotropically shaped particles and investigation of their optical and electronic properties have gained attention because of their potential applications. From a fundamental scientific understanding, nanoparticles with tailored architecture (such as core-shell) may demonstrate unique properties including quantum confinement, nonlinear optical response, blue shift, etc. Devices assembled from nanoparticles can be used in fields such as photonics, electronics, chemical sensors, photochemical processing and cosmetics.**1** Particles with core-shell structure often exhibit improved physical and chemical properties compared to their single-component counterparts, and hence are potentially useful in a broad range of applications. **2** In this thesis research, the starting materials for studying the intrinsic optical properties of the fine particles are α-Fe_2O_3 (hematite), tabular SiO_2 and Ag/SiO_2 nanocomposites. Hematite demonstrates strong absorption in the entire visible spectrum, **3** and its apparent color is determined to a large degree by particle size. **4** Ferric ions (Fe^{3+}) have also been widely used as a near infrared luminescent activator in a number of matrices. **5, 6, 7** Concentrated Fe^{3+} ions with octahedral coordination show a lack of luminescence due to the so-called "concentration quenching" effect. **8** Nanosized silica and metal/silica nanocomposites have been

extensively studied due to their electronic, optical and catalytic properties. **9, 10** Unfortunately, the nanoparticle suspensions involved were most likely stabilized by surfactant coatings, which could affect the homogeneity and optical properties of the nanoparticles arrays in the subsequent processing steps. **1** Moreover, the state of dispersion for the nanoparticle suspensions was not completely understood. Therefore, processing of nanoscale stable suspension with less residual surfactant remains a challenge. **11** The objective of this research can be divided into two parts. The first part is to prepare well dispersed Fe_2O_3, SiO_2 and Ag/SiO_2 nanocomposites from nanometer to submicrometer sizes using hydrothermal synthesis, self-assembly bilayers and reverse micelle techniques. **12, 13, 14** The second part is to assess the optical properties of the synthesized particles thereby to optimize the parameters that determine the size, shape and optical properties of the desired particles. The following work will concentrate on studying the optical behavior of the as-synthesized particles, consisting of Raman spectroscopy and UV-vis diffuse reflectance spectroscopy on materials with fully characterized sizes and shapes combined with calculations based on absorption and dynamic light scattering theory. **15, 16** The interpretation of the data acquired could establish a fundamental understanding of the optical properties for particulate materials which may reflect the role of morphology as well as atomic scale structural disorder. These efforts may provide useful guidelines for prediction of the macroscopic optical appearance of particulate materials.

2.2 Optical Properties of Ferric Oxide (Hematite) Particles

Iron oxides are a group of common metal oxides which are abundant in nature and readily synthesized in the laboratory. There are sixteen types of iron oxides, **17** among which α-Fe_2O_3 is the most stable phase and the alternate name "Hematite" derives from the Greek word *haimatos* (blood), an illusion to its striking maroon color. **17** Hematite particles are one of the most popular colored pigments that have been used in applications such as paints, cosmetics and catalysts for quite a long time. Hematite belongs to corundum structure, space group $R\bar{3}c$, in which central Fe^{3+} occupies the center of the O^{2-} octahedral groups. **18** Even though naturally occurring hematite is widespread in rocks and soils, the variance of its morphology is quite limited. **19** Through hydrothermal synthesis, however, the shape and size of hematite crystals were remarkably broadened. Matijevic *et al.* **20** pioneered the morphological manipulation of monodispersed hematite particles via a forced hydrolysis process in very dilute solutions. More recently, Sugimoto *et al* **21, 22, 23** used a gel-sol technique to process elongated shaped hematite particles from concentrated solution. The well-known morphologies for hematite particles include isotropic (spheres, cubes, pseudocubes) and anisotropic forms (ellipsoids, peanut, platelets, polyhedra), **24** ,**25** all of which can be readily synthesized by changing complexing agents, ferric salt concentration, precursor pH and temperatures. **17**

Optical properties of hematite particles were noticed to some extent to be shape and size-dependent over the past decades, but systematical comparison of optical properties with respect to particle morphology was not well established. In general, the

color of hematite powders was summarized as brownish red to iron-black in the mineralogy community. **18** , **19** , **26** , **27** The color of colloidal hematite was noticed by Kerker *et al* **28** and by Hsu **29** to be morphology dependent. Hund later compared the color of red α-Fe_2O_3 particles with respect to parameters such as particle shape, size and size distribution. It was found that the scattering and absorption cross-section behave differently when hematite particle size is less than 1.0 μm. The color purity is sensitive to particle size and shape. However, the studies were limited to small hematite particles (< 1.0 μm) with needle-like and cubic shapes. **30** By performing theoretical calculations and experimental determination on ellipsoidal hematite particles deposited as thick films, Ryde and Matijevic revealed that the color purity of nonspherical particles depends on their specific dimensional characteristics, and the relationship of the particle morphology to optical properties appears to be quite complicated. **4** However, the optical properties, particularly the color of hematite, have not been systematically compared on a fundamental basis. It is essential to measure the spectroscopic behavior of hematite so as to obtain better insight of the optical properties. Diffuse reflectance spectra were a proven technique for hematite and therefore received extensive studies from ultraviolet to near infrared region. **31** , **32** , **33** The spectra of hematite typically consist of three distinct regions: crystal field transitions at near infrared wavelengths (1200 to 700 nm), strong absorption at visible wavelengths (700 nm to 400 nm), and intense ligand to metal charge-transfer (LMCT) transitions from 400 to 200 nm. **3** , **34**

In the spectral range where crystal field transitions are the dominant mechanism, a characteristic absorption peak for hematite is associated with the $^6A_1 \rightarrow {}^4T_1$ transition at

850 nm. Adjacent to this broad band is a shoulder band at around 775 nm, caused by the $^6A_1 \rightarrow {}^4T_2$ transition. These transitions are generally spin-forbidden would be expected to be weak, but in hematite their intensities are enhanced due to magnetic coupling of two neighbor Fe^{3+} ions in the crystal structure. **35** , **36** , **37** Other crystal field transitions observed between 400 to 700 nm were assigned based on the Tanabe-Sugano diagram (Figure **2-1**) for d^5 ions by Baily, **31** Marusak **3** and Sherman. **34** In the ultraviolet region, most of the transitions occurred due to the ligand to metal charge-transfer (LMCT). Discrepancies of band assignments were found between these ill-defined bands. This may be due to increased light scattering at shorter wavelengths. **34** , **17**

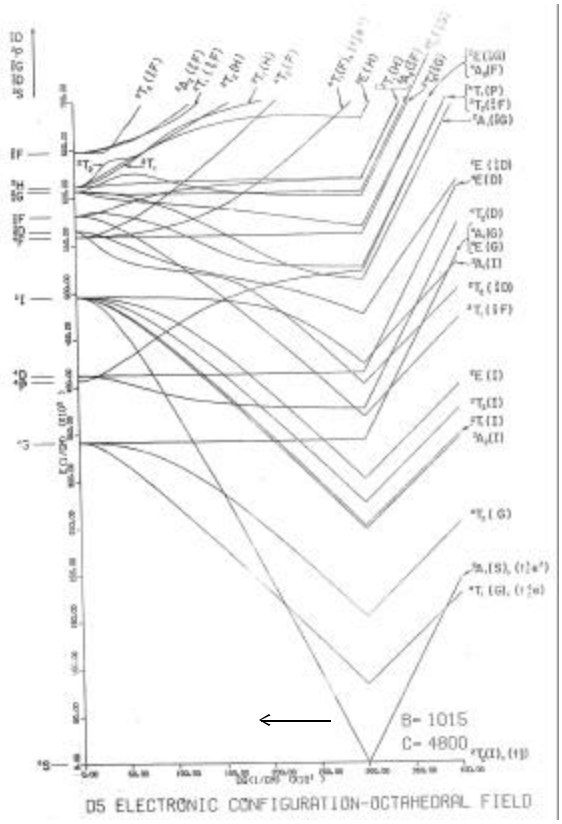

Figure **2-1**: The Tanabe-Sugano diagram for d^5 ions. Note the ground state for Fe^{3+} is $^6A_1$, B and C are the Racah constants. Left to the turning point is for high spin state, which is the case of α-Fe_2O_3. [35] (Diagram by J. S. Berkes, MRL monograph, 1968).

Raman scattering of electromagnetic radiation by hematite was extensively studied in the past few decades. The spectra measured under different conditions could provide complementary structure information to that from infrared spectra. **38** , **39** The Raman active lines of hematite were calculated based on group theory and confirmed experimentally. There are 2 A_{1g} modes and 5 E_g modes. **17** The pressure dependence of Raman active modes was also explored first by Massey *et al*. **40** and recently by Shim. **41** Although the Raman spectra of hematite predicted by group theory has been well understood and utilized to identify crystal phase behavior between various forms of iron oxides, an ambiguity regarding the origin of a peak at 1320 cm^{-1} still exits. Hart and Martin **38** attributed this to a two-magnon scattering process while McCarty, **42** Massey **40** and Shim **41** proposed a resonance enhanced two-phonon process.

The Luminescent emission of Fe^{3+} doped compounds is well known. A number of materials were proved to be suitable hosts for Fe^{3+} ions. **5** , **6** , **7** Generally Fe^{3+} activator replaces Al^{3+} at concentrations of only a few mole percent. The Fe^{3+} ion appearing in tetrahedral sites shows emission wavelength in the deep red to near infrared depending somewhat on specific values of D_q and the Stokes shift, with AlF_3 an exception. **43** For the Fe^{3+} ion locates in octahedral site, the fluorescent emission is shifted deeper into the infrared. **44** More recently, luminescence reported in nanocrystalline α-Fe_2O_3 in the visible-range was proposed to be due to surface states. **45**

2.3 Optical Properties of Silica-Based Nanocomposite

The interest in colloidal nanoparticles stems from their unique properties (optical, electrical, mechanical and chemical) that demonstrate size dependence. Following Faraday's seminal experiments on optical properties of gold nanoparticles, the knowledge of nanoparticles has been continuously expanded and enriched both fundamentally and practically. **46** More recently, intense effort has been placed on the production of composite nanoparticle with a core-shell architecture. **1**, **11** , **47** The core-shell structured nanocomposites consist of a metallic or semiconductor quantum dot that capped with a number of materials having distinctly different characteristics than the core material. The uniformly coated shell provides enhancement to the core along with passivation and extra functionalities. **10** Particularly for silica capped metallic quantum dot nanocomposites, the optical nonlinear response appears to be enhanced by size quantization and local field enhancement at the surface plasmon resonance. **11**

The optical properties of colloidal nanoparticle have been of interest for centuries. Mie had developed a fundamental theory to describe the optical properties for spherical particle, complementing classical Rayleigh scattering. **48** , **15** , **16** The Mie theory has remained an important explanation for most colloidal particle with approximately spherical geometry. However, with the development of more complicated nanoparticle systems, especially the presence of high aspect ratio nanoparticles, the optical anisotropy due to asymmetric shape should no longer be ignored. **49** , **50** , **1** Colloidal Ag nanoparticles is one of the materials demonstrate unique optical properties as a result of shape effect. The surface plasmon resonance of spherical Ag nanoparticles is at around

400 nm, however, it is split into three peaks (335, 430 and 670 nm) for trigonal Ag nanosized prism. This experimental observation has been explained by a more specific electrostatic theory that takes shape and size into consideration. **50**

The optical properties for metal-doped glasses having composite geometry were first considered by Maxwell-Garnett. **51** , **49** The original Maxwell-Garnett model assumed that the embedded particles were spherical with uniform size (Figure **2-2**). The size of the inclusion was much smaller than the typical spacing between inclusions. Similar models were also developed later to describe the composite materials by Genzel and Martin **52** for nonabsorbing medium, and by Neeves **53** for nanospheres suspened in nonlinear medium. However, a more useful approach is to express the average polarization in the inclusion under an applied electric field, **49** , **52** , **1** which is defined by Equation **2.1**

$$4pP = f(e_i - 1)E_i + (1 - f)(e_m - 1)E_m \qquad (\mathbf{2.1})$$

Where P is the average polarization, ε_i the dielectric constant for inclusion, ε_m dielectric constant for medium, *f* volume fraction inclusion, E_i and E_m are the electric field in the inclusion and medium, respectively.

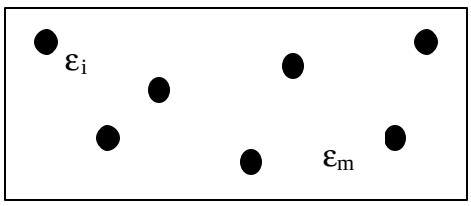

Figure **2-2**: The Maxwell-Garnett composite geometry. The dielectric constant of the inclusion is ε_i, and ε_m is the medium dielectric constant. It assumed that the inclusion particles are spherical and uniform in size. [51]

From the above equation an expression for the effective dielectric constant $\tilde{e}$ can be derived in Equation **2.2**

$$\tilde{e} = e_m \frac{e_i(1+2f)+2e_m(1-f)}{e_i(1-f)+e_m(2+f)} \qquad (\mathbf{2.2})$$

Taking Equation 2.2 to the lowest order in the fill fraction, the effective dielectric constant $\tilde{e}$ is simplified to Equation **2.3**

$$\tilde{e} = e_m + 3e_m \cdot f \frac{e_i - e_m}{e_i + 2e_m} \qquad (\mathbf{2.3})$$

The refractive index of the composite materials can now be calculated using the Maxwell relation ($\varepsilon = n^2$) that connects the dielectric constant to the index of refraction.

The unique optical properties of SiO_2 coated core-shell nanocomposites originated from the core and the SiO_2 shell enhancement. **54** , **55** For a metallic core, this enhancement displays in the surface plasmon resonance. For example, the Maxwell-Garnett model was applied to understand the dipole coupling of the surface plasmon mode in Au for a thin film deposited by Au/SiO_2 nanoparticles. The transmitted color of this thin film exhibits size dependence of the core and the shell. **56** Quantum size effect is observed in Au/SiO_2, Ag/SiO_2 and CdS/SiO_2 nanocomposites. The absorption of the CdS quantum dots is improved after silica coating. **1** More recently, the principle of surface enhanced Raman scattering has been used to improve the Raman output of a SiO_2 coated Au or Ag nanocomposites so that it can be used as a Raman tagging system in biological application. **57**

In addition to the spherical core-shell nanocomposites, a continuous SiO_2 matrix can also be utilized as a host material for creating heterogeneous structures with desired

properties. The SiO_2 substrate is chemically inert and can be loaded with guest species including metals, polymers and semiconductors. The cluster geometry can be well defined by the host microstructure. A number of nanoparticles with interesting electrical, optical and catalytic properties have been successfully embedded into mesoporous (pore size between 2 ~ 50 nm) and microporous (pore size less than 2 nm) SiO_2 frameworks. **58** There are a variety of shapes for SiO_2 matrix that may be used for host-guest inclusion, including isotropic and anisotropic particles such as spheres, fiber, and rod. However, information on formation mechanisms and crystal structural details of the cluster and physical properties of the hybrid materials are still inadequate. Besides, the inclusion of noble metal clusters such as Au, Pd and Pt in the microporous SiO_2 could lead to a distinct type of nanocomposites with unique functionalities. **59** , **60**

2.4 Conclusions

The intention of this thesis research is the fundamental understanding of optical properties of particulate materials down to nanoscale, and the study of their macroscopic morphology that may have impact on optical properties. It is necessary to address several issues so that the accomplishment of this goal is feasible. Therefore submicron size hematite particles with various morphologies were synthesized and their optical properties carefully compared using numerical techniques (Chapter 3). With these findings from a model submicron scale system, an extension will be applied to the nanosized particles. The optical properties of core-shell structured Ag/SiO_2 nanocomposites demonstrate size dependence, but dispersion of the nanocomposites

needs to be improved. To fulfill this prerequisite, a number of conventional methods were studied and agglomeration states for the suspension were determined (Chapter 4). The familiarity with the conventional methods eventually enables a dispersion scheme to be developed for silica-based nanoparticles using HPLC (Chapter 5). Further investigation of nanosized anisotropic SiO_2 particles was carried out using the knowledge on self-assembly bilayer systems. Infiltration of micropores may lead to new physical properties and open up potential applications in relevant fields (Chapter 6).

2.5 References

1. J.H. Adair, T. Li, T. Kido, K. Havey, J. Moon, J. Mecholsky, A. Morrone, D.R. Talham and M. H. Ludwig and L. Wang, "Recent developments in the preparation and properties of nanosize spherical and platelet-shaped particles and composite particles," *Materials Sci. & Eng. R*, **23** [4-5] 139-242 (1998).

2. F. Caruso, "Nanoengineering of particle surfaces," *Adv. Mater.*, **13** [1], 11-22, (2001).

3. L.A. Marusak, R. Messier and W.B White, "Optical absorption spectrum of hematite, α-Fe_2O_3 near IR to UV," *J. Phys. Chem. Solids*., **41,** 981-984 (1980).

4. N. Ryder and E. Matijevic, Color effects of uniform colloidal particles of different morphologies packed into films. *Applied Optics*, **33**(31) 7275-7281, (1994).

5. N.T. Melamed, F.S. Barros, P.J. Viccaro and J.O. Artman, "Optical properties of Fe^{3+} in ordered and disordered $LiAl_5O_8$," *Phys. Rev. B.*, **5** [9] 3377-3387 (1972).

6. J. G. Rabatin, "Luminescence of iron-activated lithium metagallate," *J. Electrochem. Soc.*, **125** [6] 920-922 (1978).

7. A. Hoffmann, R. Heitz and I. Broser, "Fe^{3+} as near-infrared luminescence center in ZnS," *Phys. Rev. B.*, **41** [9] 5806-5815 (1990).

8. T. Abritta, F. S. Barros and N. T. Melamed, "Luminescence of Fe^{3+} in single crystal of $LiAl_5O_8$," *J. Lumin.*, **33**, 141-146 (1985).

9. T. Li, J. Moon, A.A. Morrone, J. J. Mecholsky, D. R. Talham and J. H. Adair, "Preparation of Ag/SiO_2 nanosize composites by a reverse micelle and sol-gel technique, " *Langmuir*, **15** [13] 4328-4334 (1999).

10. P. Mulvaney, L.M. Liz-Marzan, M. Giersig and T. Ung, "Silica encapsulation of quantum dots and metal clusters," *J. Mater. Chem.*, **10**, 1259-1270 (2000).

11. J. H. Fendler, "Self-assembled nanostructured materials," *Chem. Mater.*, **8**, 1616-1624 (1996).

12. J. Sjoblom and P. Stenius, "Phase equilibria of nonionic surfactants and the formation of microemulsions," pp. 369-433 in Surfactant Science Series, Vol. 23, *Nonionic Surfactant*, Edited by M. J. Schick, Marcel Dekker, Inc, New York, 1987.

13. A. W. Ralston, C. W. Hoere and E. J. Hoffman, "Studies on high molecular weight aliphatic amines and their salts. VII. The systems octylamine-, dodecylamine- and octadecylamine-water," *J. Am. Chem. Soc.*, **64**, 1516-1523, (1942).

14. J. Wang, W. B. White and J. H. Adair, "Synthesis and characterization of tabular silica nanoparticles," *Proceedings for Fine Powder Processing 2001*, pp. 242-248, Penn State, PA, 2001.

15. C.F. Bohren and D.R. Huffman, *Absorption and scattering of light by small particles*, John Wiley & Sons, Inc, New York, 1998.

16. M. Kerker, *The scattering of light and other electromagnetic radiation*, Academic Press, New York, 1969.

17. R. M. Cornell and U. Schwertman, *"The Iron Oxides: Properties, Reactions, Occurrences and Uses"*; 2nd edition, VCH, New York, 2003.

18. J. W. Anthony, R. A. Bideaux, K. W. Bladh and M. C. Nichols, *Handbook of mineralogy, Vol III, halides, hydroxides, oxides*. Mineral Data Publishing, Tucson, AZ, 1990.

19. E. S. Dana, The system of mineralogy of James Dwight Dana, pp213-215, John Wiley & Sons, New York, 1903.

20. E. Matijevic and P. Scheiner, Ferric hydrous oxide sols. III. "Preparation of uniform particles by hydrolysis of Fe(III)-Chloride, Nitrate, and –Perchlorate solutions." *J. Colloid Interface Sci*. **63**[3], 509-524, (1978).

21. T. Sugimoto and K. Sakata, "Preparation of monodisperse pseudocube α-Fe_2O_3 particles from condensed ferric hydroxide gel." *J. Colloid Interface Sci*. **152**[2], 587-590, (1992).

22. T. Sugimoto, A. Muramatsu, K. Sakata and D. Shindo, "Characterization of hematite particles of different shapes," *J. Colloid Interface Sci*. **158**, 420-428, (1993).

23. T. Sugimoto, M. M. Khan and A. Muramatsu, "Preparation of monodisperse peanut-type α-Fe_2O_3 particles from condensed ferric hydroxide gel," *Colloid and Surfaces A*, **70**, 167-169, (1993).

24 M. P. Morales, T. G. Carreno and C. J. Serna, "The formation of α-Fe_2O_3 monodispersed particles in solution," *J. Mater. Res.* **7**[9], 2538-2545, (1992).

25 Q. Liu, "Synthesis of monodispersed hematite particles from highly concentrated solutions," Ph. D thesis, The Pennsylvania State University, 2002.

26. U. Schwertman and R. M. Cornell, "Iron oxides in the laboratory," 2nd edition, Wiley-VCH, New York, 2000.

27. T. C. Patton, "Pigment handbook, Volume II, applications and markets." Wiley-Interscience, New York, 1973.

28. M. Kerker, P. Scheiner, D. D. Cooke and J. P. Kratohvil, "Absorption index and color of colloidal hematite," *J. Colloid Interface Sci.*, **71**, 176-187, (1979).

29. W. P. Hsu and E. Matijevic, "Optical properties of monodispersed hematite hydrosols," *Appl. Opt.* **24**, 1623-1630, (1985).

30. F. Hund, "Inorganic pigment: Bases for colored, uncolored, and transparent products", *Angew. Chem. Int. Ed. Engl.* **20**, 723-730, (1981).

31. P. C. Bailey, "Absorption and reflectivity measurements on some rare earth Iron garnets and α-Fe_2O_3". *J. Appl. Phys.*, **31,** 39S-40S, (1960).

32. S. P. Tandon and J. P. Gupta, "Diffuse reflectance spectrum of ferric oxide". *Spec. Lett*. **3,** 297-301, (1970).

33. D. M. Sherman, R. G. Burns and V. M. Burns, Spectral characteristic of the iron oxides with application to the Martian bright region mineralogy," *J. Geophys. Res.*, **87**, 10169-10180, (1982).

34. D. M. Sherman, T. D. Waite, "Electronic spectra of Fe^{3+} oxides and oxide hydroxides in the near IR to near UV". *American Mineralogist*, **70**, 1262-1269, (1985).

35. A. B. P. Lever, "Inorganic Electronic Spectroscopy," Elsevier, New York, 1968.

36. G. Blasse and B. C. Grabmaier, "Luminescent Materials," Springer-Verlag, New York, 1994.

37. D. M. Sherman, The electronic structure of Fe^{3+} coordination sites in Iron Oxides: Application to spectra, bond, and magnetism," *Phys. Chem. Minerals*, **12**, 161-175, (1985).

38. T. P. Martin, R. Merlin, D.R. Huffman and M. Cardona, "Resonant two magnon Raman scattering in Fe_2O_3," *Solid State Commun.* **22,** 565-567, (1977).

39. R. L. Farrow and A. S. Nagelberg, "Raman spectroscopy of surface oxides at elevated temperature," *Appl. Phys. Lett*., **36**[12], 945-947, (1980)

40. M.J. Massey, U. Baier, R. Merlin and W.H. Weber, "Effects of pressure and isotopic substitution on the Raman spectrum of α-Fe_2O_3: Identification of two-magnon scattering," *Phys. Rev. B: Condensed Matter*, **41,** 7822-7827, (1990).

41. S. H. Shim and T. S. Duffy, "Raman spectroscopy of Fe_2O_3 to 62 GPa," *American Mineralogist,* **87**, 318-326, (2001).

42. K. F. McCarty, "Inelastic scattering in α-Fe_2O_3: phonon vs magnon scattering," *Solid State Communications*, **68**, 799-802, (1988).

43. D.J. Telfer and G. Walker, "Fe^{3+} luminescence center in Aluminium Fluoride," *J. Lumin.*, **11,** 315-320, (1976).

44. K. E. Fox, T. Furukawa and W. B. White, "Luminescence of Fe^{3+} in metaphosphate classes: Evidence for four and six-coordinated sites," *J. Am. Ceram. Soc.*, **64,** C-42-43, (1981).

45. B. S. Zuo, V. Volkov, "Surface modification on time-resolved fluorescence of Fe_2O_3 nanocrystals," *J. Phys. Chem. Solids*, **61**, 757-764, (2000).

46. D. J. Schiffrin, Capped nanoparticles as potential electronic components with nanoscale dimensions," MRS Bulletin. **26**[12], 1015-1019, (2001).

47. L. M. Liz-Marzan, M. Giersig and P. Mulvaney, "Synthesis of nanosized gold-silica core-shell particles," *Langmuir*, **12**, 4329-4335, (1996).

48 G. Mie, "Beitrage zur optik truber medien, speziell kolloidaler metallosungen," *Ann. Phys.*, **25**, 377-355, (1908).

49. R. Gehr and R. W. Boyd, "Optical properties of nanostructured optical materials," *Chem. Mater.*, **8**, 1807-1819, (1996).

50. K. L. Kelly, E. Coronado, L. L. Zhao and G. C. Schatz, "The optical properties of metal nanoparticles: the influence of size, shape and dielectric environment," *J. Phys. Chem. B.*, **107**, 668-677, (2003).

51. J. C. Maxwell Garnett, "Colours in metal glasses and in metallic films," *Philos. Trans. R. Soc.*, **203**, 385-420, (1904).

52. L. Genzel and T. P. Martin, "Infrared absorption by surface phonons and surface plasmons in small crystal," *Surface Sci.*, **34**, 33-49, (1973).

53. A. E. Neeves and M. H. Birnboim, "Composite structure for the enhancement of nonlinear optical materials," *Optics Lett.*, **13**, 1087-1089, (1988).

54. C. G. Granqvist and O. Hunderi, "Optical properties of Ag-SiO_2 cermet films: A comparison of effective-medium theories," *Phys. Rev. B.*, **18**, 2897-2906, (1978).

55. G. L. Fischer and R. W. Boyd, "Third-order nonlinear optical properties of selected composites," *Nanostructured Materials, ACS Symposium Series*, **679**, 108-124, (1997).

56. T. Ung, L. M. Liz-Marzan and P. Mulvaney, "Optical properties of thin films of Au@SiO_2 particles," *J. Phys. Chem. B*, **105**, 3441-3452, (2001).

57. S. P. Mulvaney, M. D. Musick, C. D. Keating and M. J. Natan, "Glass-coated, analyte-tagged nanoparticles: A new tagging system based on detection with surface-enhanced Raman scattering," *Langmuir*, **19**, 4784-4790, (2003).

58. G. D. Stucky and J. E. MacDougall, "Quantum confinement and host/guest chemistry: probing a new Dimension,' *Science*, **247**, 669-678, (1990).

59. A. T. Bell, "The impact of nanoscience on heterogeneous catalysis," *Science*, **299**, 1688-1691, (2003).

60 D. R. Rolison, "Catalytic nanoarchitectures- the importance of nothing and the unimportance of periodicity," *Science*, **299**, 1698-1701, (2003).

Chapter 3

Synthesis and Optical Properties of Hematite Particles

3.1 Introduction

Iron oxide (α-Fe_2O_3, hematite) particles have attracted much interest for many years due to their various geometrical shapes and unique optical and magnetic properties. **1** , **2** From the materials synthesis point of view, different shapes of hematite particles have been obtained by carefully controlling processing parameters. **3** Hydrothermal synthesis was found to be an effective approach to manipulate the size and shape of the hematite particles. **2** , **4** , **5** For example, Ozaki *et al*. **2** prepared platelet-like hematite particles by introducing ethylenediaminetetraacetate (EDTA) into a Teflon-liner autoclave containing ferric hydroxide precursor. The particles formed single magnetic domains. A systematic study on growth mechanism of hematite particles produced by hydrothermal treatment was reported by Sugimoto and coworkers. **3** , **4** It was found that adsorption of ions such as Cl^{1}, SO_4^{2-} and PO_4^{3-} plays an important role in the nucleation and growth of hematite. Peanut-like, cubic or spindle-like particles were obtained in the presence of various ions.

As a traditional pigment being used in many applications, the optical properties of hematite have been studied extensively. **1** However, most work done in this regard did not provide enough information on particle size and shape related to macroscopic optical properties. One of the striking optical properties for hematite is its color, which was

known for years but not studied in detail until the work by Kerker *et al*., **6** Hsu *et al*. **7** for colloidal hematite, with Hund, **8** Ryde and Matijevic **9** who correlated the color to particle size and shape (cubes, spheres and needles). More recently, Katsuki and Komarneni **5** , **10** extended this effort to the nanosize scale by comparing the colors of hematite particles generated from microwave synthesis. According to the optical absorption study of hematite thin films by Marusak *et al.* **11** α-Fe_2O_3 strongly absorbs over the entire visible spectrum range. However, questions remain on the effect of particle size and shape on the optical absorption and scattering behavior of hematite pigments. **12**

Luminescent materials activated by transition metal ions generally exhibit concentration quenching at concentrations of a few mole percent. However, the expected effect was not observed in the case of small α-Fe_2O_3 particles. Fe^{3+} has the d^5-electron configuration. It is isoelectronic with the well-known activator Mn^{2+} but the higher charge shifts Dq to higher values and thus the luminescent $^4T_1 \rightarrow {}^6A_1$ transition shifts to lower wavenumbers. Fe^{3+} is frequently used as a luminescent dopant. Compounds exhibiting Fe^{3+} emission include $LiAlO_2$, **13** $LiGaO_2$, **14** $LiAl_5O_8$, **13** , **15** , **16** , **17** , **18** $LiGa_5O_8$, **18** AlF_3, **19** $KAlSi_3O_8$, **20** Zn_2SiO_4, **21** ZnS, **22** , **23** $CuGaS_2$, **24** $CuAlS_2$, **24** and phosphate **25** and aluminosilicate **26** glasses. There are several common themes to these compounds. One is that the Fe^{3+} activator replaces Al^{3+} at concentrations of only a few mole percent. The other is that (except for AlF_3) the Fe^{3+} appears in tetrahedral coordination with its emission wavelength in the deep red to near-infrared depending somewhat on specific values of Dq and the Stokes shift. The few examples known of emission of Fe^{3+} on octahedral sites include AlF_3 **19** and some phosphate glasses. **25**

Emission from octahedral Fe^{3+} is shifted deeper into the infrared, often at or beyond the cutoff for the detectors used in the spectrometers. A report on nanocrystalline Fe_2O_3 luminescence described visible-range emission which was ascribed mainly to surface states. **27**

The intent of this chapter is to prepare hematite particles with controlled shape and size via hydrothermal synthesis and to determine the optical properties as a function of size and shape. Another emphasis will be on a weak near infrared luminescence of the submicrometer trigonal corundum-type structured Fe_2O_3 particles with Fe^{3+} coordinated by face-sharing octahedra. The objective is to achieve a fundamental understanding of the mechanisms behind the pigment coloration.

3.2 Experimental Procedure

3.2.1 Synthesis of Hematite Platelets

The typical procedure used to prepare hematite platelet particles initially reported by Matijevic **2** is summarized in Figure 3-1. Amorphous $Fe(OH)_xO_y$ precipitates were first obtained by mixing 2 mL 0.5 M $FeCl_3$ ($FeCl_3 \cdot 6H_2O$, Aldrich Chemical Co., Milwaukee, WI) with 6 mL 4 M NaOH (J. T. Baker, Phillipsburg, NJ) aqueous solution, and 8 mL 0.2 M EDTA (Aldrich Chemical Co., Milwaukee, WI). Two mL 2 M NaCl (J. T. Baker, Phillipsburg, NJ) was added up to a total solution of 18 mL. The highly alkaline suspension was then transferred into a 23 mL stainless steel acid digestion bomb (Parr Instrument, Moline, IL) lined with Teflon and heat treated at 180 °C for more than 6 h. The precipitated particles were washed with 0.001 M HNO_3 (J. T. Baker, Phillipsburg,

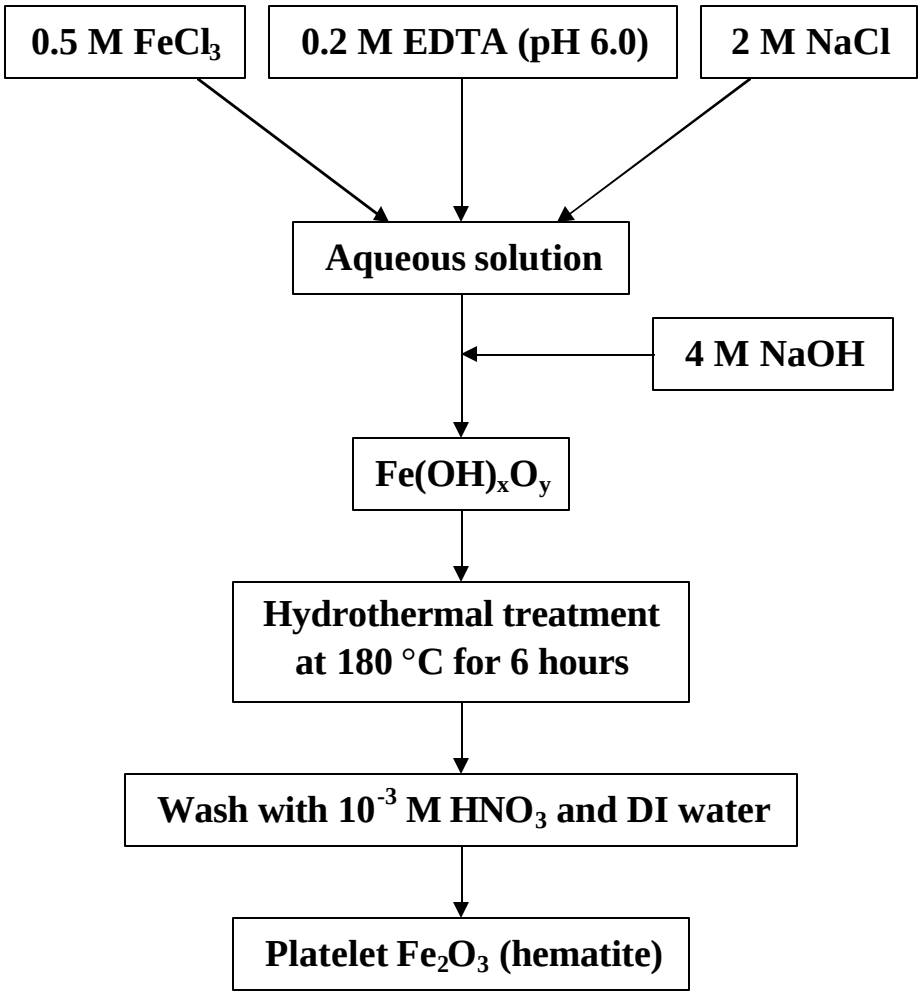

Figure 3-1 Flow sheet for hydrothermal synthesis of hematite platelet. Procedure was described by Matijevic *et al.* [2] for platelet and Sugimoto *et al.* [4, 28] for pseudocube and peanut-like particles.

NJ) solution 3 times followed by deionized water 5 times (specific conductivity = 0.4×10^{-7} S/m). The particles were redispersed in DI water with a result of pH 6.0. The final suspension of Fe_2O_3 platelet particles had a purple color.

3.2.2 Synthesis of Polyhedron Hematite Particles

The procedure to prepare polyhedron Fe_2O_3 particles is different from the method to prepare platelets. The $Fe(OH)_xO_y$ precursor was first obtained by mixing 200 mL 0.5 M $FeCl_3$ with 600 mL 0.5 M NaOH and aged at room temperature overnight. The precipitate was centrifuged at 1500 rpm for 5 minutes and the $Fe(OH)_xO_y$ gel was collected and dispersed in DI water. The pH of the suspension was adjusted to pH 12.0 with a total volume of 480 mL. The final suspension was transferred to a 600 mL hydrothermal vessel and heated at 180°C for 10 hours with a continuous stirring rate of 150 rpm. The product was washed and redispersed in a manner similar to that used for hematite platelets.

3.2.3 Synthesis of Anisotropic Hematite Particles

Using the same starting chemicals, pseudocubic and peanut-like hematite particles were prepared following the protocol described by Sugimoto. **4** , **28** Initially, 10 mL 2 M $FeCl_3$ was directly mixed with 9 mL 6 M NaOH with the solution diluted to a total volume of 20 mL by DI water. After stirring for 5 minutes, the solution was transferred to the 23 mL Teflon-lined hydrothermal vessel and heat treated at 100°C for 8 days. For

peanut-like particles, 1 mL of 0.6 M Na_2SO_4 stock solution (Aldrich Chemicals Co. Milwaukee, WI) was used instead of DI water.

3.2.4 Characterization

The morphology of the hematite particles was determined by scanning electron microscope (SEM, Hitachi S-3000H, Tokyo, Japan). Phase identification was done by X-ray diffraction (Scintag, Inc., Cupertino, CA, Cu Ka with a wavelength of 1.5418 Å). The surface charge of the hematite particles in aqueous was determined by Zeta PALS Analyzer based on the dynamic light scattering principle (Brookhaven Instruments Co., NY).

The shape of the hematite particles is strongly determined by the processing techniques and the parameters involved. **28** Figure 3-2 shows the morphology of Fe_2O_3 particles hydrothermally treated at 180°C and 100°C, respectively. If the $Fe(OH)_xO_y$ precipitates were aged first prior to hydrothermal treatment, the growth of platelet hematite particles is believed to proceed through a dissolution-recrystallization mechanism from β-FeOOH. **3** , **4** The basal plane diameter of the platelets in Figure 3-2 is about 3 μm and the thickness is around 0.5 μm, giving an aspect ratio of 6. The platelet particles possess a pseudohexagonal shape. The basal plane is the {0001} face and the side plane is the $\{01\bar{1}2\}$ face according to Sugimoto. **4** The characteristic shape of the platelet was formed due to stronger adsorption of OH^- to the {0001} faces thereby retarding the growth in this direction. The growth rate on $\{01\bar{1}2\}$ is relatively fast resulting in a tabular shape. The formation of hematite polyhedra was primarily due to

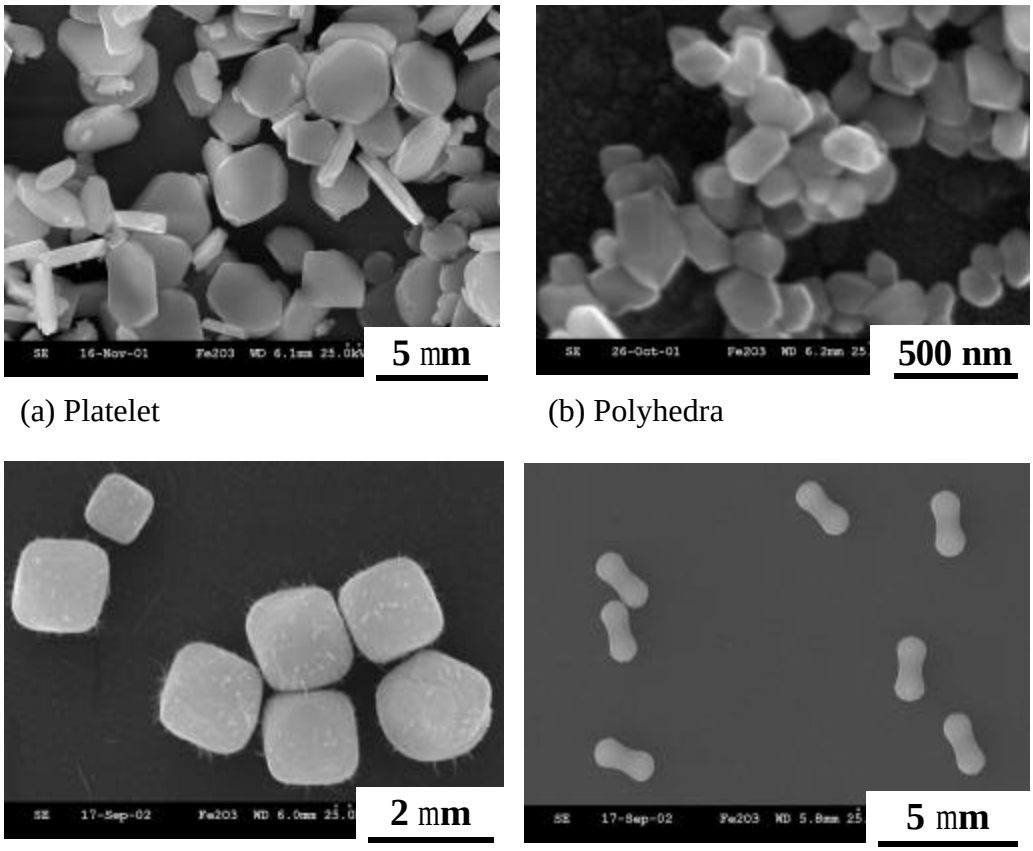

(a) Platelet (b) Polyhedra

(c) Pseudocube (d) Peanut-like

Figure 3-2 SEM micrograph of hematite particles prepared by hydrothermal synthesis. (a) Platelets, 180°C, 6h, with 0.2 M EDTA; (b) Polyhedra, 180°C, 10h; (c) Pseudocube, 100°C, 8 days; (d) Peanut-like, 100°C, 8 days, with 0.6 M Na_2SO_4.

the lack of preferred growth direction in the recrystallization step. In the case of pseudocubic hematite, the adsorption of Cl^- or chloro ferric complexes on the $\{01\bar{1}2\}$ faces is responsible for the restrained growth in the directions normal to the $\{01\bar{1}2\}$ faces. The presence of sulfate retarded the growth of crystal planes parallel to the c axis and forced the hematite particles to form an elongated peanut shape. A detailed discussion on the growth mechanisms for anisotropic hematite particles is postulated by Sugimoto **3** and Liu **29** elsewhere.

The XRD pattern shows that at a 3-hour heat treatment, both goethite (JCPDS ICDD 29-713) and hematite (JCPDS ICDD 33-664) are present, which is confirmed by SEM analysis. Goethite particles convert to hematite platelets with longer reaction time. XRD data for the 6-hour sample shows a pure hematite phase. No additional phase transformation is disclosed at longer holding times, which suggests the heating time for preparation of hematite particles should be no less than 6 hours. A complete comparison of the XRD patterns showed single-phase hematite for all morphologies (Figure 3-3). The diffraction lines for the platelets were very sharp while those for the polyhedra pseudocubic and peanut-like particles were somewhat broadened indicating less crystallinity.

To further modify the particle shape, samples were hydrothermally treated at 24 and 48 hours under the same conditions, respectively as for the 3 and 6 hours runs. According to the SEM observations, the particle shape was similar to those obtained at 6 hours (Figure 3-2), which indicates that longer heating times does not change the shape of the platelet. Previous studies show that different ions such as Cl^-[1] and SO_4^{2-} can

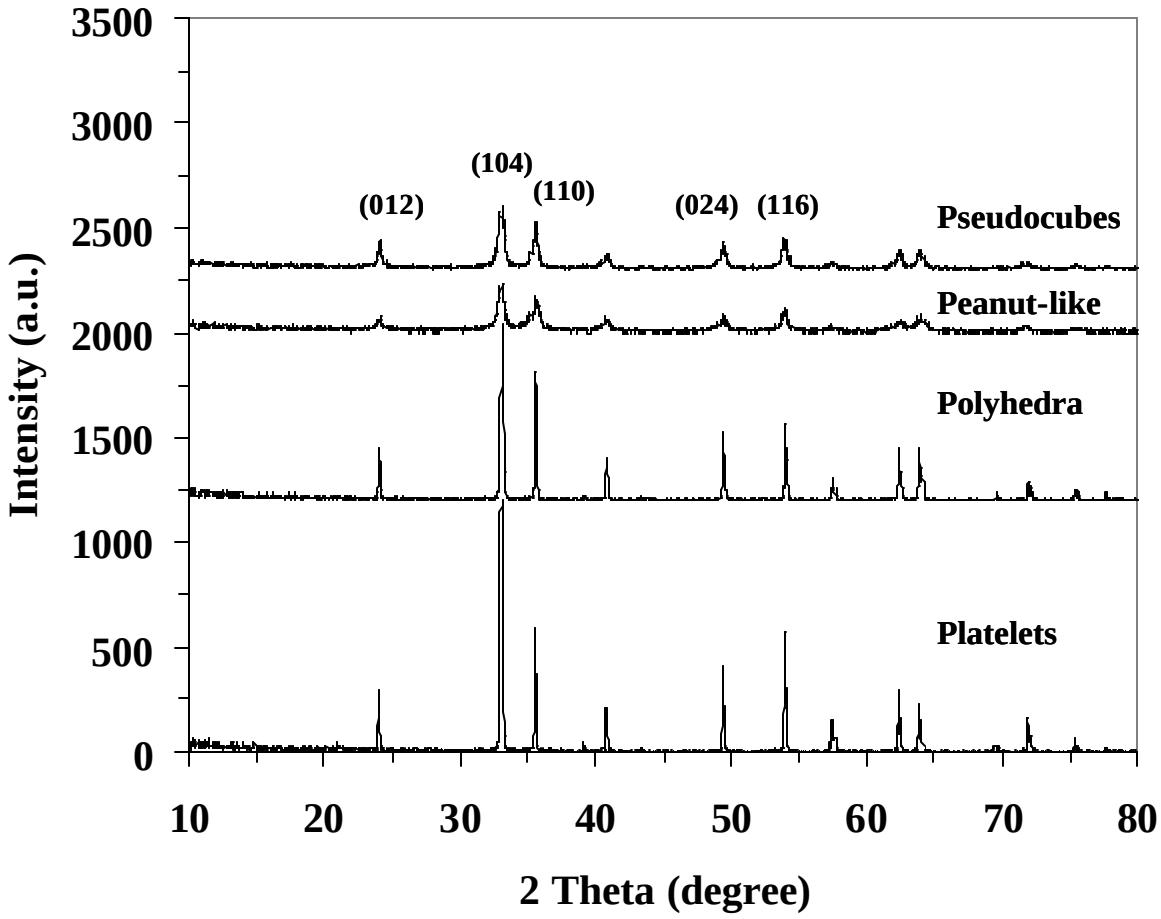

Figure 3-3 X-ray diffraction patterns for hematite particles. Note increased diffraction line widths in the sequence platelets → polyherda → pseudocubes and peanut-like. Hematite phase JCPDS ICDD 33-664.

strongly determine the shape of hematite particles. **3** , **30** The residual Cl^{-1} ions in the system may play a role in the evolution of hematite platelet particles during hydrothermal treatment.

The isoelectric point (IEP) of hematite particles dispersed in DI water exhibits morphology dependence (Figure 3-4), a similar effect was observed by Bell *et al*. **31** in the system of gylcothermally synthesized α-Al_2O_3 particles. Hematite platelets show an IEP around pH 8.2, while the IEP for polyhedron particles is shifted to pH 10.6. The difference of cation to anion ratio on a specific crystal planes was ascribed to the origin of this shift.

A commercially available hematite powder obtained from The Estee Lauder Corporation was used in the study of optical properties for hematite pigments. The particle size of The Estee Lauder sample was determined to be 0.5 μm with a random morphology and high purity (99.9%).

3.3 Optical Properties

3.3.1 Color

The apparent color of Fe_2O_3 particles significantly depends on phase, size and possibly the shape of particles. Hematite particles with a size around 0.3 μm have a strong maroon color, while platelet particles show a purple color with particle size about 3 μm. For a more precise comparison of the apparent color of the hematite particles, Munsell color notation was utilized. The Munsell notation uses hue (position of color in the spectrum, red, green, blue, etc.), lightness (on a scale ranging from black to white)

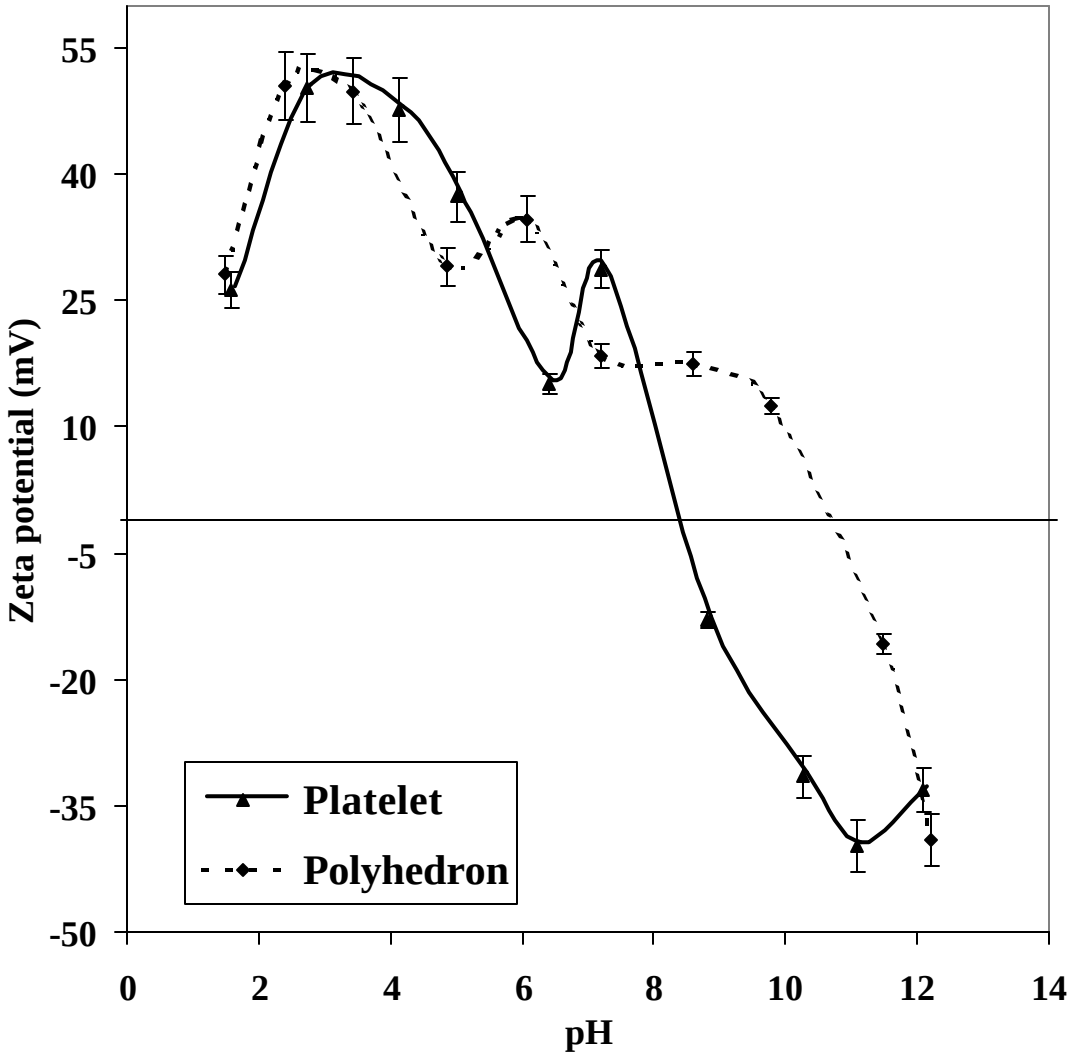

Figure 3-4 Zeta potential of hematite particles as a function of pH. The pH of the Fe_2O_3 aqueous suspensions were adjusted with 0.1 M HNO_3 and 0.1 M NaOH. The isoelectric point (IEP) is pH 8.2 for platelet and pH 10.6 for polyhedron. Error bars are the 95% confidence interval.

and saturation (the purity of the hue going from the grey to the pure color) to identify color using the notation hue value/chroma (H V/C) (Figure 3-5). **32** It is interchangeable with other color systems such as the CIE (International Commission on Illumination) system through computer-aided transfer. **1** , **33** Hematite particles were dried on a glass slide and compared with the Munsell color chips (Table 3-1). Hematite platelet particles (3 μm × 0.5 μm) have a purple color (10R 4/1), while the Munsell color notation for hematite polyhedra clearly depends on particle size. The hue, value and chroma change as the particle size increases.

3.3.2 Reflectance Spectra

Diffuse reflectance spectra of hematite particles were obtained by a Perkin Elmer Lambda 900 UV-vis-NIR spectrometer with $BaSO_4$ used as a reference material. The reflectance of hematite particles were also evaluated by means of a Datacolor SF 600 CT spectrophotometer (Estee Lauder, NY), a 31-point measurement was taken in the visible region from 400 to 700 nm.

The effect of particle size and shape on the color of hematite is illustrated by the reflectance spectra from 400 to 700 nm (Figure 3-6). The hematite particles have a very low reflectance from 400 to 570 nm. A rapid increase of reflectance occurs at about 570 nm. The slope of the curve depends on the particle size and shape involved. Polyhedron particles generally show higher reflectance than platelets when the incident wavelength is higher than 570 nm, and the degree of increase is strongly related to particle size for the same geometrical shape. Smaller polyhedron particles usually display a steep rise in

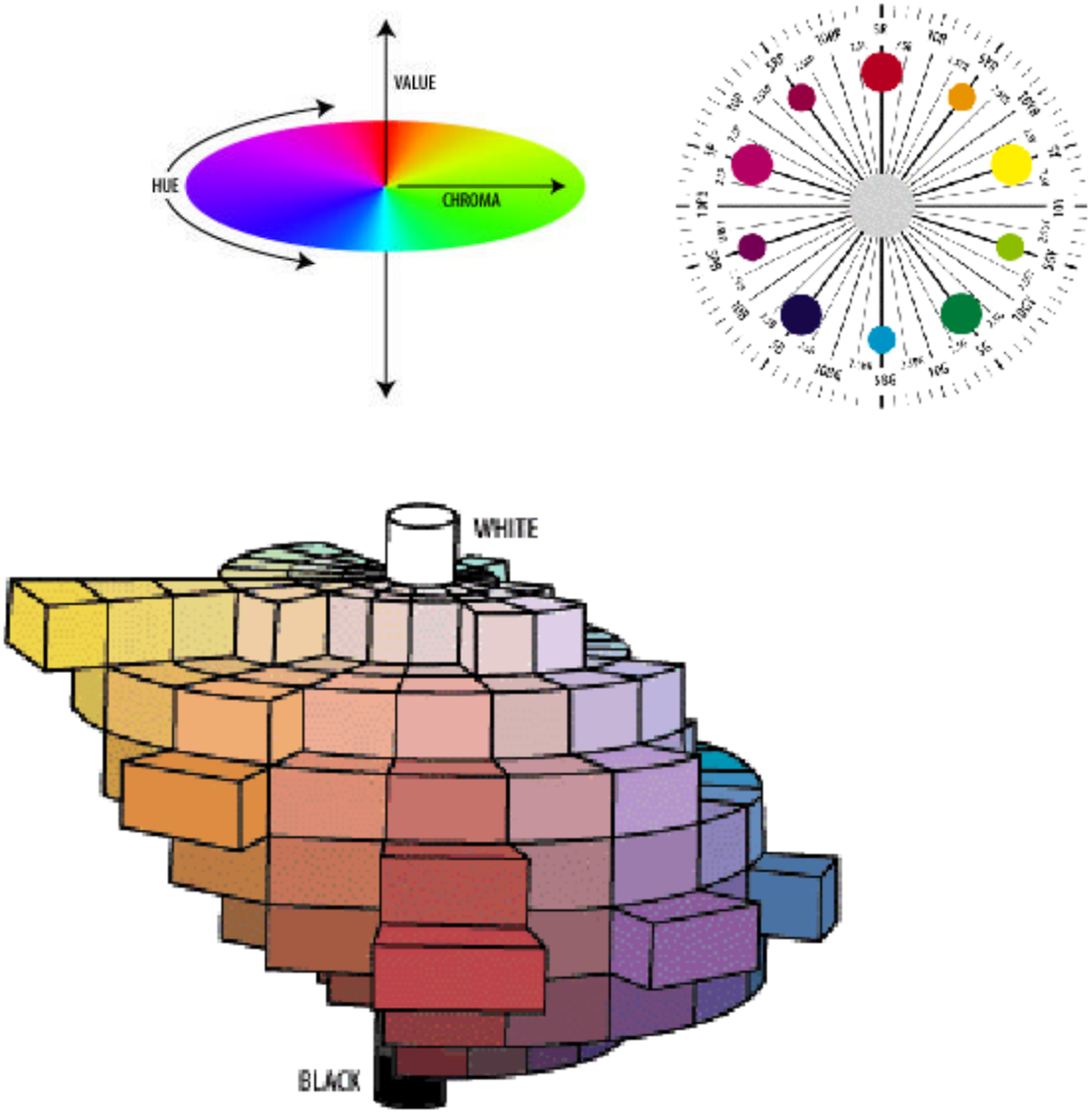

Firgure 3-5 Munsell color notation. The cylindrical coordinates of the Munsell color notation (top left), the hue notation (top right) and the 3D view of the Munsell color space consist of color chips (bottom). (Figures from Munsell, a division of Gretag Macbeth, LLC.)

Table 3-1 Munsell color notation of hydrothermally synthesized hematite particles

Sample ID	Parameters	Size (μm)	Shape	H V/C	Color chip
Hematite	180°C, 6h	3.0 × 0.5	Platelet	10R 4/1	
Hematite	180°C, 24h	3.0 × 0.5	Platelet	10R 4/1	
Hematite	180°C, 10h	0.2	Polyhedron	7.5R 4/8	
Hematite	180°C, 10h	0.3	Polyhedron	5R 4/2	
Hematite	180°C, 14h	0.5	Polyhedron	5R 4/8	
Hematite	180°C, 20h	1.0	Polyhedron	5R 5/8	
Hematite	As-received	0.5	Random	5R 5/8	

Note: The Munsell notation uses hue (H), value or lightness (V) and chroma or purity of color (C) to identify color using the notation hue value/chroma (H V/C). Hue basically refers to the spectral colors red (R), yellow (Y), green (G), blue (B), purple (P) and their intermediates. Value changes from 0 (black) to 10 (white). Chroma increases from 0 in steps of one, the higher the C value, the purer the color.

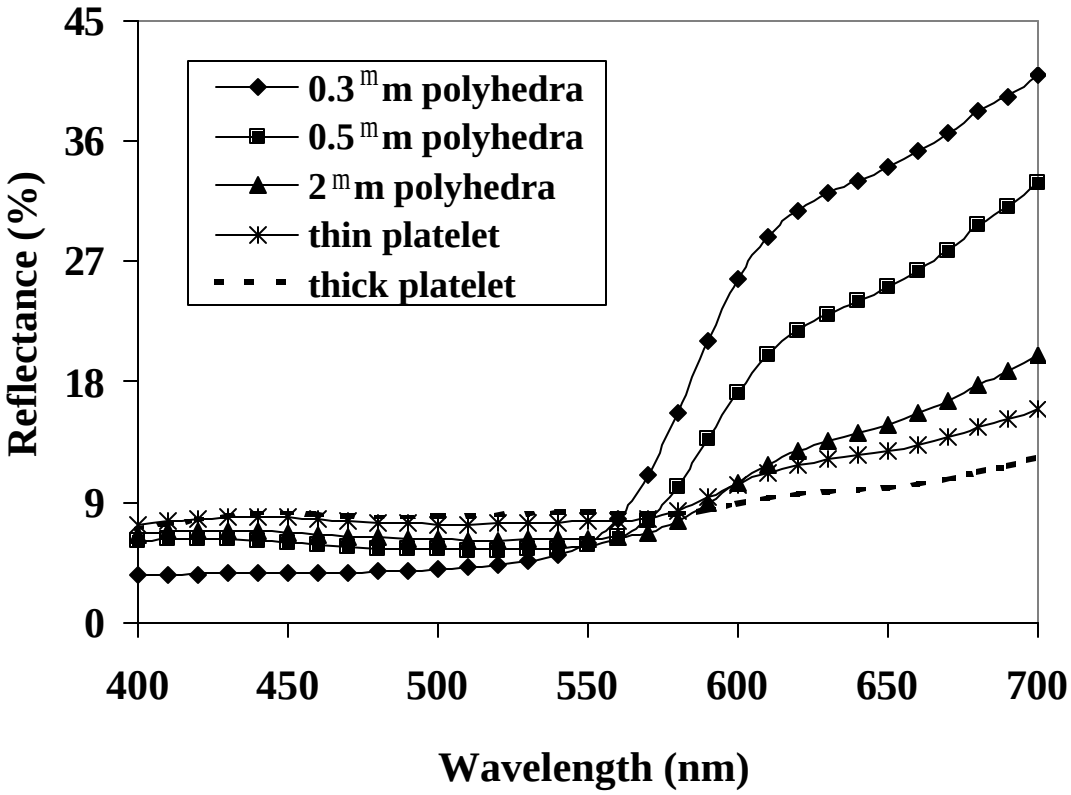

Figure 3-6 Reflectance spectra of hematite particles in the visible spectrum. The reflectance of hematite increases as particle size decreases from 570 to 700 nm, and platelets show lower reflectance than that of polyhedra.

reflectance from 550 to 600 nm that gives the particles their red color. A near-flat reflectance curve for platelets accounts for the purple color observed since most incoming light was absorbed by the material.

Diffuse reflectance spectra of α-Fe_2O_3 particles are presented in Figure 3-7. Based on the data obtained in this work and on literature available regarding the optical absorption spectra of hematite, **11** , **34** , **35** , **36** , **37** the observed peaks can be assigned as following:

(1) The near infrared range from 700 nm to 1200 nm. This is a relatively low absorption region occupied by recognizable crystal field bands. A distinct band observed at 850 nm (11765 cm^{-1}) in polyhedron and 3 μm platelet hematite particles is due to the $^6A_1 \rightarrow {}^4T_1$ ligand field transition. Marusak and coworkers **11** observed this band at 11560 cm^{-1}, while Tandon and Gupta **34** reported a value of 11630 cm^{-1}. In this work, only one broad band was recorded for the polyhedron and platelet hematite in the wavelength range from 700 nm to 900 nm. However, this broad band is split into two bands for pseudocubic and peanut like particles. As shown in the inserted figure, the two bands occur at about 820 nm and 890 nm, respectively. The peak at 890 nm most likely corresponds to the $^6A_1 \rightarrow {}^4T_1$ transition, and another spin forbidden transition from $^6A_1 \rightarrow {}^4T_2$ may give rise to the band at 820 nm (12195 cm^{-1}), as was recorded in hematite thin films at 12900 cm^{-1} by Marusak *et al*. **11** even though the assignment is not certain. Although these bands can be assigned to crystal field transition, their intensities are much higher than that expected for purely crystal effects.

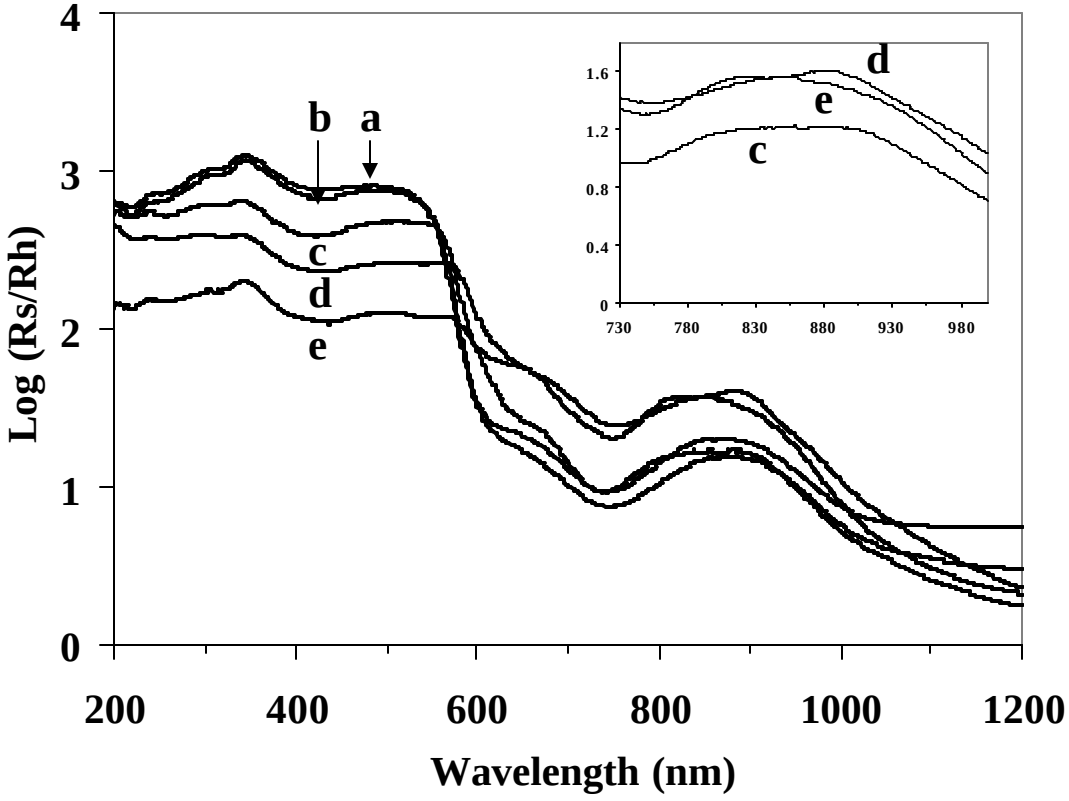

Figure 3-7 Diffuse reflectance spectra of hematite particles prepared by hydrothermal synthesis. (a) Polyhedra; (b) As-received; (c) Peanut-like; (d) Pseudocube; (e) Platelet. Note the shift of optical absorption edge at about 570 nm when particle morphology varies. The single broad band at 850 nm is split into two bands (820 and 890 nm) for pseudocube and peanut-like hematite particles. Baseline is obtained by a standard $BaSO_4$ sample. Rs-reflectance of $BaSO_4$, Rh-reflectance of hematite.

(2) Visible spectrum from 400 nm to 700 nm. There is a significant shape dependence of the spectra. Three poorly-defined absorption bands at 650 nm (15385 cm^{-1}), 535 nm (18691 cm^{-1}) and 470 nm (21276 cm^{-1}) were observed in this region. The first two bands at 650 nm and 535 nm are believed to arise from spin-forbidden ligand field transitions and have been observed previously by Marusak *et al*. **11** and Sherman, **36** even though the band assignment given by them was not identical. The third absorption band at 470 nm is assigned to the spin-flip transition among the $2t_{2g}$ states. **11** , **35** Sherman observed this band at 430 nm and assigned it to the $^6A_1 \rightarrow {}^4E$ transition. **36** However, two of these bands shift to longer wavelengths in the anisotropic particles, similar to the so-called "red shift". Consequently, this shift increases the wavelength of each band by a value of about 40 nm, so that absorption bands were observed at 570 nm (17544 cm^{-1}) and 510 nm (19608 cm^{-1}), respectively. The complete set of observed transitions and assignments are summarized in Table 3-2.

(3) Ultraviolet region from 200 to 400 nm. Three weak absorption features superimposed on a very intense background can be identified at 330 nm (30303 cm^{-1}), 290 nm (34483 cm^{-1}) and 230 nm (43478 cm^{-1}). Very little detail can be resolved. These bands have been attributed to ligand-to-metal charge transfer between the O_{2p} orbitals to the Fe^{3+} $2t_{2g}$ and $3e_g$ orbitals. **11**

(4) Absorption edge. The optical gap obtained from the diffuse reflectance spectra of hematite polyhedra is about 2.22 eV (560 nm) and 2.14 eV (580 nm) for platelet particles. The agreement is good with the band gap reported in literature. **38** , **39** , **40** The origin for the shift between the two particle sizes is not clear at the present time.

Table 3-2 Summary of the absorption bands and assignments in hematite, α-Fe_2O_3

This work (cm^{-1})	Assignment	Marusak	Sherman	Tandon & Gupta
11765(P, T)	$^6A_1 \rightarrow {}^4T_1$	11560	11000	11630
15385 (P, T)	$^6A_1 \rightarrow {}^4A_1$	16670	15000	--
18691 (P) 17544 (T)	$^6A_1 \rightarrow {}^4E$	18690	18180	--
21276 (P) 19608 (T)	$2t_{2g} \uparrow \rightarrow 2t_{2g} \downarrow$	20408	20800	21500
30303 (P, T)	$1t_{1u} \downarrow \rightarrow 2t_{2g} \downarrow$	31750	27780	28570
34483 (P, T)	$1t_{1g} \downarrow \rightarrow 3e_g \downarrow$	38900	34480	34480
43478 (P, T)	$6t_{1u} \downarrow \rightarrow 3e_g \downarrow$	44840	--	43290

Note: P = polyhedra, T = platelet, pseudocube and peanut-like.

The spectra were acquired by scanning a layer of hematite particles deposited on an Aluminum sample holder with $BaSO_4$ used as a reference material.

The vibrational terms A, E, T are defined by group theory.

3.3.3 Raman Spectra

A Bomem DA3+ FT Raman spectrometer was employed to measure the Raman scattering of hematite. Excitation was by a 600 mW YAG laser source with a wavelength of 1064 nm. InGaAs was used as the detector. Raman spectra of platelet particles were also obtained with a microRaman spectrometer using an Ar-Kr gas laser with a power of 200 mW.

Raman spectra were measured on commercial hematite powder by McCarty *et al*. **41** at ambient conditions, and by Shim *et al*. **42** at high pressure. Seven Raman active lines were observed and assigned based on a group theory calculation. Hematite belongs to $R\bar{3}c$ space group with a corundum type structure. **1** Based on group theory predications, there should be seven Raman active vibrational modes which include 2 A_{1g} modes and 5 E_g modes. The present spectra are shown in Figure 3-8. Although there still exist some differences regarding the position and intensity of each Raman-active line, the general trend is that the seven vibrational modes span from about 220 cm^{-1} to 620 cm^{-1}. There are two strong Raman lines, one A_{1g} mode at 225 cm^{-1} and one E_g mode at 293 cm^{-1}. Table 3-3 summarizes the vibrational bands and assignments on this work in comparison with the results reported in literature. **43** , **44** Hematite platelet particles have somewhat different spectra from polyhedron particles in response to incoming 1064 nm excitation. Seven Raman lines were observed in hematite platelets, with the vibrational frequencies in good agreement with literature. However, the spectral profile changes in the hematite polyhedron as size decreases. Six Raman lines were observed. The intensity

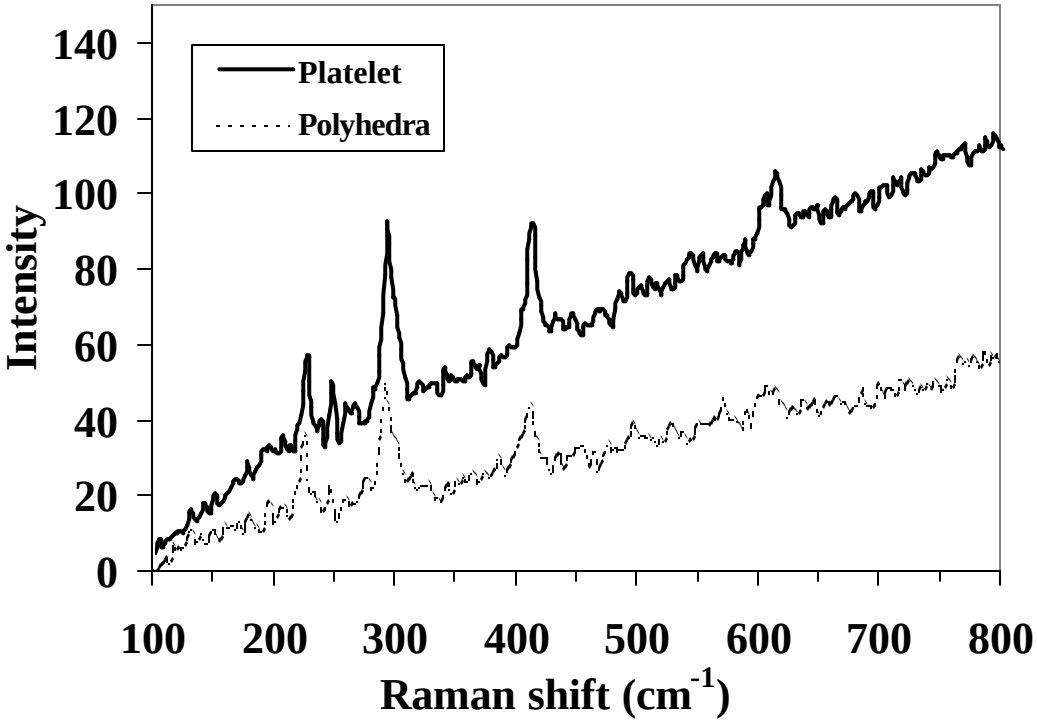

Figure 3-8 Raman spectra of hematite particles prepared by hydrothermal synthesis. The excitation was by a 0.6 W YAG laser source (λ = 1.064 μm). Note platelets show higher scattering intensity than that of polyhedra.

Table 3-3 Assignment of vibrational modes for hematite particles

Mode (cm^{-1})	Platelets	Polyhedra	Shim	Massey
A_{1g}	226	226	224	228
E_g	247	247	243	246
E_g	292	293	290	294
E_g	298	299	297	300
E_g	412	413	408	412
A_{1g}	493	--	496	496
E_g	614	616	609	614

Note: The Raman spectra were acquired by scanning the hematite particles deposited on a zero background glass slide under ambient condition.

The A_{1g} mode at 496 cm^{-1} was not observed in the case of hematite polyhedra.

of the vibrational bands decreases as frequency increases, which eventually leads to a low intensity of the A_{1g} mode at 493 cm^{-1} and the E_g mode at 614 cm^{-1}.

Raman spectra of Fe_2O_3 prove to be very sensitive to excitation wavelength (Figure 3-9). The line shapes and band intensities for platelet particles were significantly dependent on excitation wavelength. When the laser line changes from blue (457 nm) to green (514 nm), the Raman active modes remain the same except a slight decrease of intensity. However, when yellow line (568 nm) and red line (647 nm) were used, the Raman spectra are quite different in many features. With 568 nm excitation, the peak at about 1320 cm^{-1} was strongly enhanced and there was enhanced intensity for all Raman lines. The Raman spectra become most sharp and intense when excited by the red line, although the peak at 1320 cm^{-1} completely disappeared. The low intensity for the Raman spectra under blue and green can be expected due to the strong absorption of incoming radiation with a wavelength shorter than the optical absorption edge of hematite, which is around 570 nm for platelet particles. The red line, 647 nm, falls exactly on the optical absorption edge so that the great intensity enhancement is due to resonance scattering. However, the explanation to the wavelength response behavior of the peak at 1320 cm^{-1} is still unclear. Although this band had been observed previously, ambiguity still exists about its origin. Martin proposed a two magnon scattering process. **44** Other work by McCarty, **41** Massey *et al.* **43** and Shim and Duffy **42** support a resonance-enhanced two-phonon scattering process. The very sharp frequency response shown in Figure 3-6 suggests that a specific electronic transition along the optical absorption edge is responsible for the resonance coupling. The fundamental mode would be 660 cm^{-1} and would be connect to an IR-active vibration.

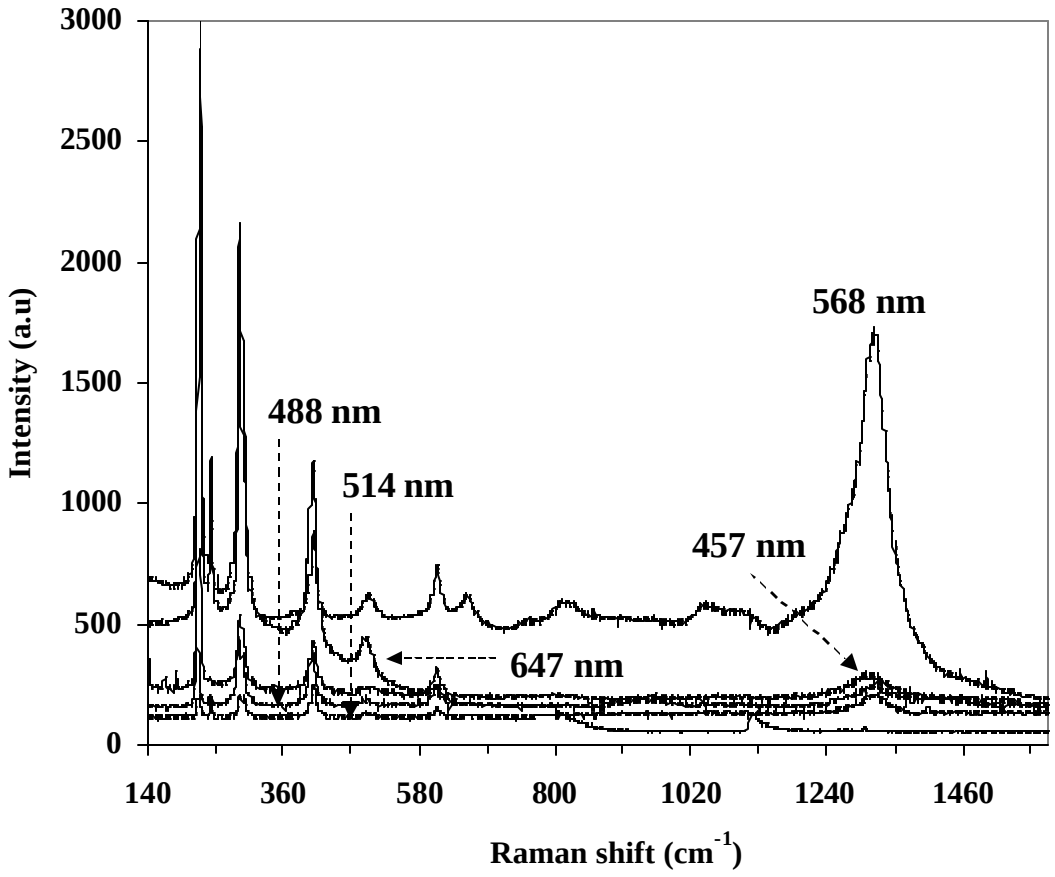

Figure 3-9 Raman spectra of hematite platelet particles with various excitation wavelengths. Spectra acquired by a microRaman spectrometer using an Ar-Kr gas laser with an output of 200 mW. The intensity enhancement in 568 and 647 nm excitations is due to resonance Raman scattering (Absorption edge of hematite platelet is 580 nm).

3.3.4 Luminescent Spectra

Luminescence of all types of hematite particles was excited using a Nd:YAG laser producing 600 mW power at 1064 nm in combination with a BOMEM DA^{3+} Fourier transform Raman spectrometer. The InGaAs detector has an effective cutoff at 1650 nm so the abrupt decrease in intensity at the low frequency end of the spectra probably represents the sensitivity limit of the detector. The hematite powders were placed between two pieces of zero-background glass slides and properly aligned before each scan.

Emission spectra of the as-prepared particles are shown in Figure 3-10. Some sense of the intensity of the broad band emission may be obtained by comparison with the sharp, high wavenumber bands which are the Raman lines of hematite. There are three overlapping broad bands with relative intensities that depend on the morphology of the Fe_2O_3 particles. All spectra were deconvoluted to three overlapping Gaussian lines and the fits were used to determine the wavenumber at the band maximum (Table 3-4).

There are at least four possibilities for the source of the weak infrared emission: (i) an intrinsic emission of Fe^{3+} in the Fe_2O_3 host structure. (ii) A band edge or defect emission from the hematite structure (iii) an emission from impurities in the Fe_2O_3. (iv) an emission from adsorbed impurities on the particle surfaces arising from the synthesis process.

To evaluate the possible adsorption of luminescent surface species, the platelet particles were annealed at a series of temperatures. Temperatures as high as 1000 °C

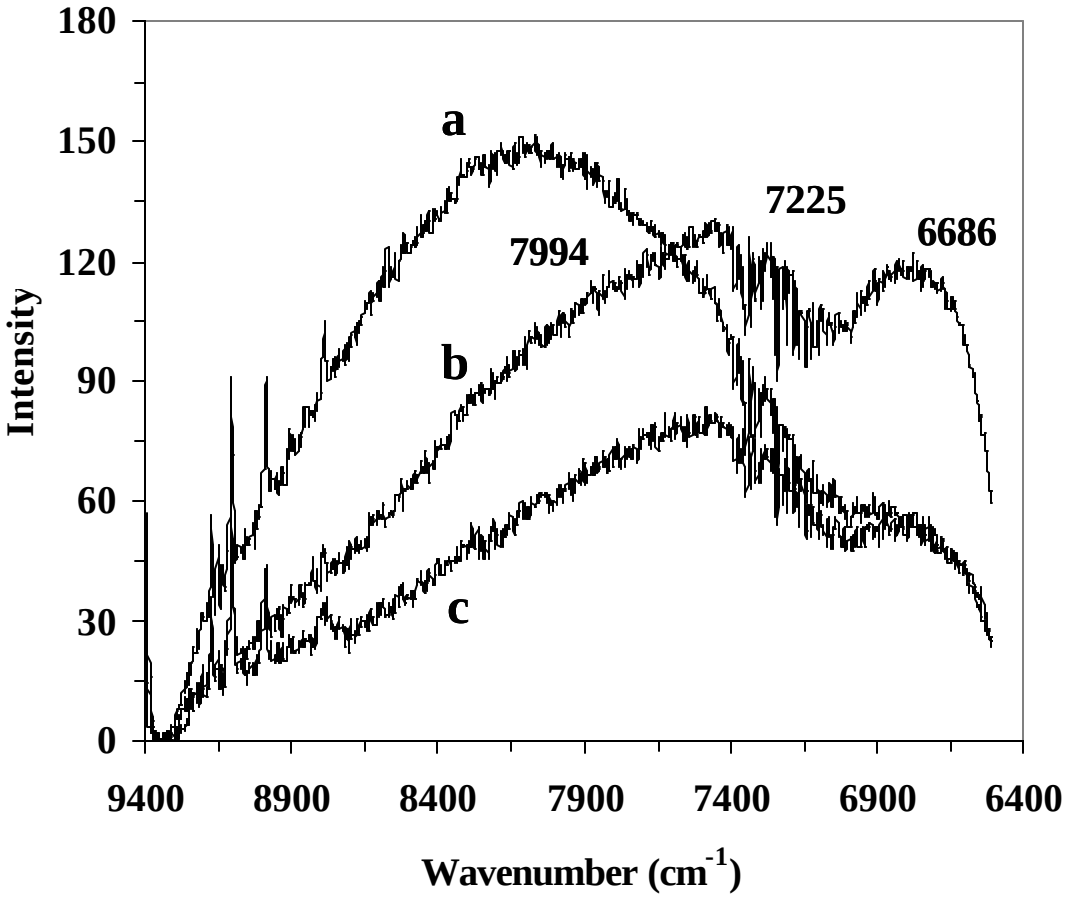

Figure 3-10 Emission spectra of hematite particles as synthesized. (a) platelets, (b) polyhedra, (c) pseudocubes. Band A = 7994 cm^{-1}, Band B = 7225 cm^{-1}, and Band C = 6686 cm^{-1} for polyhedra. Deconvoluted with PeakFit®.

Table 3-4 Emission band wavenumbers determined by fitting observed spectra. Fitting error standard deviation = 50 cm^{-1}.

Sample	Band A (cm^{-1})	Band B (cm^{-1})	Band C (cm^{-1})
Platelets, 25° C	8212	7391	6717
Platelets, 500° C	8188	7367	6698
Platelets, 1000° C	8188	7367	6698
Polyhedra	7994	7225	6685
Pseudocubes	7977	7338	6696
E-L 25° C	8236	7395	6737
E-L 300° C	8174	7395	6719
E-L 500° C	8185	7395	6702
E-L 700° C	8169	7394	6707
E-L 1000° C	8064	7411	6717

E-L = Estee Lauder

should volatilize surface species. However, the annealed particles, in fact, produced a more intense luminescence than the unannealed particles (Figure 3-11). It seems unlikely that simple adsorbed species are the source of the luminescence.

A chemical analysis (X-ray fluorescence, The Mineral Lab, CO) of the platelet particles (Table 3-5) reveals several potential activators. Mn^{2+} is a classical activator, but, especially in the annealed particles, should be in the form of Mn^{3+} in solid solution in the Fe_2O_3. Ni^{2+} is a known activator with an emission in the near infrared. **45** , **46** The emission from the $^3T_{2g} \rightarrow {}^3A_{2g}$ transition in MgO:Ni^{2+} is near 8000 cm^{-1} at 15 K. **46** The Ni^{2+} emission exhibits strong thermal quenching and at most only a very weak emission would be expected at 300 K. Because the low temperature literature spectra exhibit considerable fine structure, it is not easy to compare these spectra with the broad band emission observed in the present investigation.

To obtain an independent comparison, a sample of small particle Fe_2O_3 used in the cosmetic industry was obtained from the Estee Lauder Corporation. It also exhibited a similar weak infrared luminescence (Figure 3-12). An unexpected result is that this sample also gave a more intense luminescence after the powder had been annealed at high temperature. The bands shift to lower wavenumber with higher temperature anneals. The Estee Lauder Fe_2O_3 was of higher purity than the synthesized material (Table 3-5).

The evidence from the annealing experiments and from the comparison of spectra of Fe_2O_3 from different sources seems to eliminate possibilities (iii) and (iv). The observed luminescence appears to be an intrinsic property of Fe_2O_3.

If the emission is from Fe^{3+} in an octahedral site in Fe_2O_3, it should arise from the usual $^4T_{1g} \rightarrow {}^6A_{1g}$ transition. In single crystal Fe_2O_3 this transition has been identified at

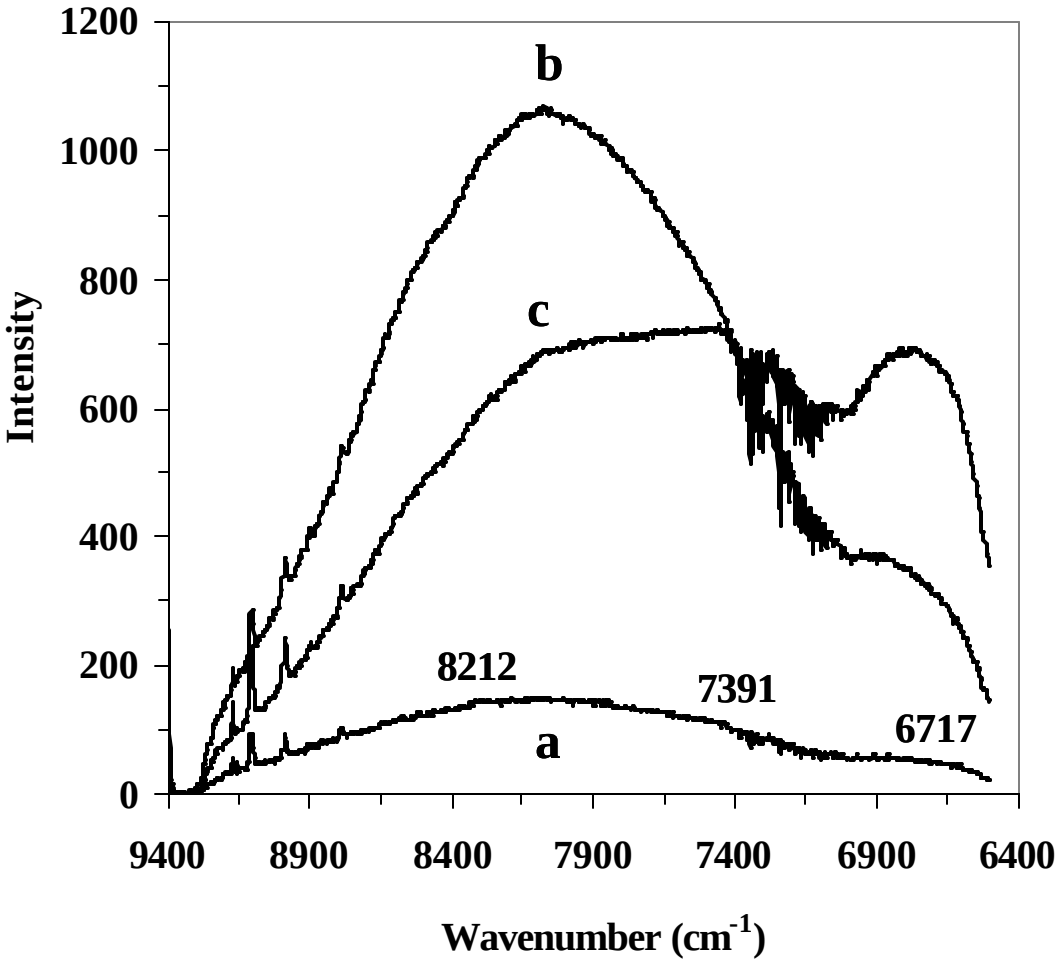

Figure 3-11 Emission spectra of hematite platelet particles after annealing at the specified temperatures. (a) unannealed, (b) 500°C, 3h, (c) 1000°C, 3h. Band A= 8212 cm^{-1}, Band B = 7391 cm^{-1}, and Band C = 6717 cm^{-1} for unannealed particles. Deconvoluted with PeakFit®.

Table 3-5 Chemical composition of platelet (Plat.) and Estee Lauder (E-L) Fe_2O_3 determined by X-ray fluorescence analysis.

Minor Elements	Plat.[a]	E-L[a]	Detection Limit	Trace Elements	Plat.[b]	E-L[b]	Detection Limit
Na_2O	Nd	nd	0.05	V	34	15	10
MgO	Nd	nd	0.05	Cr	131	42	10
Al_2O_3	Nd	nd	0.03	Co	75	nd	10
SiO_2	Nd	nd	0.03	Ni	517	76	10
P_2O_5	Nd	nd	0.05	Cu	38	38	10
S	Nd	nd	0.05	Zn	nd	11	10
Cl	0.16	nd	0.02	As	nd	nd	20
K_2O	0.27	nd	0.01	Sn	nd	nd	50
CaO	Nd	nd	0.01	Pb	nd	nd	10
TiO_2	Nd	nd	0.01	Mo	nd	nd	10
MnO	0.10	0.04	0.01	Sr	nd	nd	10
Fe_2O_3	99.1	99.94	0.01	U	nd	23	10
BaO	Nd	nd	0.01	Th	nd	19	10
				Nb	nd	nd	10
				Zr	nd	nd	10
				Rb	nd	nd	10
				Y	nd	nd	10

"Not detected", nd, is specified for those elements with concentrations less than the detection limit. (a) Concentrations in weight percent. (b) Concentrations in parts per million.

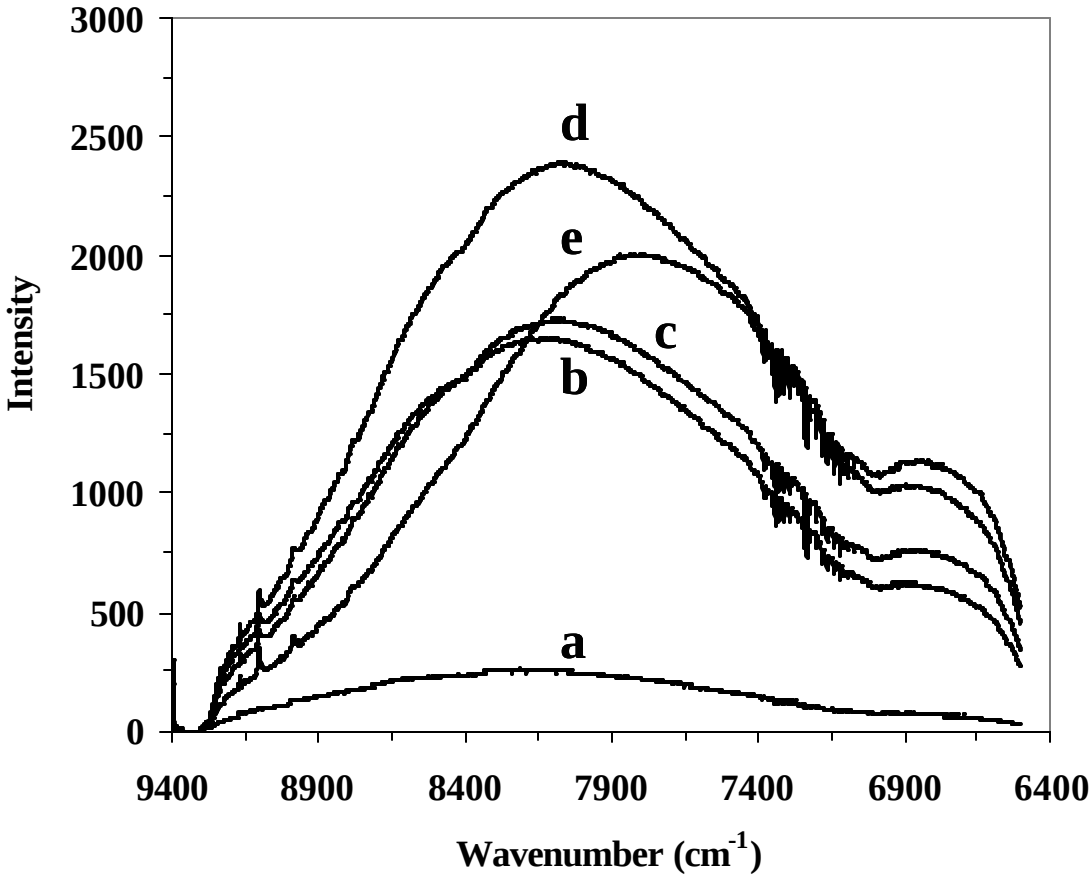

Figure 3-12 Emission spectra of commercial small particle hematite after annealing at various temperatures. (a) unannealed, (b) 300°C, 3h, (c) 500°C, 3h, (d) 700°C, 3h, (e) 1000°C, 3h. Note the weak Raman scattering peaks from 9400 cm^{-1} to 8900 cm^{-1}.

11,750 cm^{-1}. **11** The absorption coefficients of both the $^4T_{1g}$ and $^4T_{2g}$ spin-forbidden transitions is two to three orders of magnitude higher than what would be expected from pure crystal field transitions. Magnetic coupling between adjacent Fe^{3+} ions is claimed to be responsible for this effect. **36** The larger absorption coefficient of these bands would enhance pumping by the Nd:YAG laser (9400 cm^{-1}) but the emission is at a wavelength where Fe_2O_3 is relatively transparent.

Assigning the Fe_2O_3 emission bands to the $^4T_{1g} \rightarrow {}^6A_{1g}$ transition requires Stokes shifts of 3553, 4374, and 5048 cm^{-1} respectively for the three observed bands. The values are large but not impossible. There is also the problem of explaining why the emission appears as three separate bands with relative intensities that vary between the different particle morphologies. Furthermore, the shifts in emission wavenumber with temperature of annealing must be explained (Table 3-4). The obvious wavenumber shift after 1000 °C annealing might be an indication of improved crystallinity at high temperature.

The effective absorption edge for Fe_2O_3 is near 15,500 cm^{-1} (645 nm) where the absorption coefficient begins to abruptly increase from about 2000 cm^{-1} for the two crystal field bands to values in excess of 10^5 cm^{-1} in the visible region of the spectrum. **11** The observed emission bands, therefore seem to occur at too low a wavenumber to be due to exciton or electron/hole recombination at the absorption edge. The role of defects cannot be discounted. Fe_2O_3 is known to be slightly non-stoichiometric. **47** A distribution of oxygen vacancies near the emitting Fe^{3+} ions or deep traps could be responsible for the observed multiband structure of the luminescence spectrum.

3.4 Conclusions

Phase pure hematite particulate pigments with various sizes and shapes were prepared via hydrothermal treatment of $Fe(OH)_xO_y$ gel at designed conditions depending on the morphology required. Platelet-like hematite particles (3 μm × 0.5 μm) were obtained with the presence of EDTA at pH 12, while the absence of EDTA will form hematite polyhedra. The perceived colors of the pigments vary with particle size and shape. The apparent color of hematite particles changes from maroon (5R 4/2) to purple (10R 4/1) as particle size increases from 0.2 μm to 3 μm based on the Munsell color notation. A "red-shift" of the absorption bands for hematite particles were observed in platelet particles, in comparison with polyhedron-like hematite particles. The Raman band intensities of hematite particles exhibit a significant dependence on particle size, excitation source and vibrational frequency as revealed. The E_g mode at 614 cm^{-1} was significantly reduced as particle size decreases to 0.5 μm.

A weak near infrared fluorescence emission was observed in phase pure hematite polycrystal particulate powders. The as-synthesized hematite particles were stable during high temperature annealing, while the spectral intensity was significantly enhanced. The possible origins responsible for the near infrared luminescence were discussed.

3.5 References

1. R. M. Cornell and U. Schwertman, *"The Iron Oxides: Properties, Reactions, Occurrences and Uses,"* VCH, New York, pp.1-25, 1996.

2. M. Ozaki, N. Ookoshi and E. Matijevic, "Preparation and magnetic properties of uniform hematite platelets,"*J. Colloid Interface Sci.*, 1**37**, 546-549, (1990).

3. T. Sugimoto and Y. Wang, "Mechanism of the shape and structure control of monodispersed α–Fe_2O_3 particles by sulfate ions," *J. Colloid Interface Sci.*, **207**[1], 137-149, (1998).

4. T. Sugimoto, S. Waki, H. Itoh and A. Muramatsu, "Preparation of monodispersed platelet-type hematite particles from a highly condensed β–FeOOH suspension," *Colloids and Surfaces A,* **109,** 155-165, (1996).

5. H. Katsuki and S. Komarneni, "Microwave-hydrothermal synthesis of monodispersed nanophase α-Fe_2O_3," *J. Am. Ceram. Soc.,* **84**[10], 2313-2317, (2001).

6. M. Kerker, P. Scheiner, D.D. Cooke and J. P Kratohvil, "Absorption and index and color of colloidal hematite," *J Colloid and Interface Sci.,* **71**,176-187, (1979).

7. W. P. Hsu and E. Matijevic, "Optical properties of monodispersed hematite hydrosols," *Appl. Opt.* **24**, 1623-1630, (1985).

8. F. Hund, "Inorganic pigment: Bases for colored, uncolored, and transparent products," *Angew. Chem. Int. Ed. Engl.,* **20**, 723-730, (1981).

9. N. P. Ryde and E. Matijevic, "Color effects of uniform colloidal particles of different morphologies packed into films," *Appl. Opt.*, **33**[31], 7275-7281, (1994).

10. H. Katsuki and S. Komarneni, "Role of α-Fe_2O_3 morphology on the color of red pigment for porcelain". *J. Am. Ceram. Soc.,* **86**[1], 183-185, (2003).

11. L. A. Marusak, R. Messier and W. B. White, "Optical absorption spectrum of Hematite, α-Fe_2O_3 near IR to UV," *J. Phys. Chem. Solids.*, **41**, 981-984, (1980).

12. C. F. Bohren and D. R. Huffman, *Absorption and scattering of light by small particles,* John Wiley & Sons, NY, 1998.

13. D. T. Palumbo, "Electronic states of Fe^{3+} in $LiAlO_2$ and $LiAl_5O_8$ phosphors,"*J. Lumin.*, **4**, 89-97, (1971).

14. J. G. Rabatin, "Luminescence of iron-activated lithium meta gallate," *J. Electrochem. Soc.* **125**[6], 920-922, (1978).

15. P. M. Jaffe, "The cathodoluminescence spectra and coordination of Mn^{2+}, Fe^{3+} and Cr^{3+} in β-$LiAl_5O_8$," *J. Electrochem. Soc.*, **115**[11], 1203-1205, (1968).

16. N.T. Melamed, F.S. Barros, P.J. Viccaro and J.O. Artman, "Optical properties of Fe^{3+} in ordered and disordered $LiAl_5O_8$," *Phys. Rev. B.*, **5**[9], 3377-3387, (1972).

17. T. Abritta, F. S. Barros and N. T. Melamed, "Luminescence of Fe^{3+} in single crystal of $LiAl_5O_8$," *J. Lumin.*, **33**,141-146, (1985).

18. J. M. Neto, T. Abritta, F. de S. Barros and N. T. Melamed, "A comparative study of the optical properties of Fe^{3+} in ordered $LiGa_5O_8$ and $LiAl_5O_8$," *J. Lumin.*, **22**, 109-120, (1981).

19. D. J. Telfer and G. Walker, "Fe^{3+} luminescence centres in aluminum fluoride," *J. Lumin.*, **11**, 315-320, (1976).

20. W. B. White, M. Matsumura, D. G. Linnehan, T. Furukawa, and B. K. Chandrasekhar, "Absorption and luminescence of Fe^{3+} in single-crystal orthoclase," *Amer. Mineral.*, **71**, 1415-1419, (1986).

21. E. Cavalli, A. Belletti and E. Zannoni, "Luminescence of Fe-doped willemite single crystals," *J. Solid State Chem.*, **117**, 16-20, (1995).

22. P.M. Jaffe and E. Banks, "Iron activated ZnS phosphors," *J. Electrochem. Soc.*, **111**, 52-61, (1964).

23. A. Hoffmann, R. Heitz and I. Broser, "Fe^{3+} as near-infrared luminescence center in ZnS," *Phys. Rev. B.*, **41**[9], 5806-5815, (1990).

24. K. Sato and T. Teranishi, "Infrared luminescence of Fe^{3+} in $CuGaS_2$ and $CuAlS_2$," *J. Phys. Soc. Japan*, **37**, 415-422, (1974).

25. K. E. Fox, T. Furukawa and W. B. White, "Luminescence of Fe^{3+} in metaphosphate classes: Evidence for four and six-coordinated sites," *J. Am. Ceram. Soc.*, **64**, C 42-C 43, (1981).

26. D. S. Kinght and W. B. White, "Ferric ion species in alkali aluminosilicate glasses during fusion," *J. Am. Ceram. Soc.*, **71**[7], C 342-C 344, (1988).

27. B. S. Zuo and V. Volkov, "Surface modification on time-resolved fluorescences of Fe_2O_3 nanocrystals,"*J. Phys. Chem. Solids,* **61**, 757-764, (2000).

28. T. Sugimoto, A. Muramatsu, K. Sakata and D. Shindo, "Characterization of hematite particles of different shapes," *J. Colloid Interface Sci*., **158**, 420-428 (1993).

29. Q. Liu, "Synthesis of monodispersed hematite particles from highly concentrated solutions," Ph. D thesis, The Pennsylvania State University, 2002.

30. T. Sugimoto, Y. Wang, H. Itoh and A. Muramatsu, "Systematic control of size, shape and internal structure of monodisperse α-Fe_2O_3 particles," *Colloids and Surfaces A*, **134**, 265-279, (1998).

31. N. S. Bell, "Interfacial aspects of glycothermally synthesized alpha alumina," Ph.D. Thesis, The University of Florida, 1996.

32. Specifying the color by the Munsell system, *American Society for Testing and Materials,* pp.1-4, 1968.

33. U. Schwertman and R. M. Cornell, "Iron oxides in the laboratory," 2nd edition, Wiley-VCH, New York, 2000.

34. S. P. Tandon and J. P. Gupta, "Diffuse reflectance spectrum of ferric oxide," *Spec. Lett*., **3,** 297-301, (1970).

35. P. C. Bailey, "Absorption and reflectivity measurements on some rare earth Iron garnets and α-Fe_2O_3," *J. Appl. Phys.*, **31,** 39S-40S, (1960).

36. D. M. Sherman, T. D. Waite, "Electronic spectra of Fe^{3+} oxides and oxide hydroxides in the near IR to near UV," *American Mineralogist*, **70**, 1262-1269 (1985).

37. D. M. Sherman, R. G. Burns and V. M. Burns, "Spectral characteristic of the iron oxides with application to the Martian bright region mineralogy," *J. Geophys. Res.*, **87**, 10169-10180, (1982).

38. K. L. Hardee and A. J. Bard, "The application of chemically vapor deposited Iron oxide films to photosensitized electrolysis," *J. Electrochem. Soc.*, **123,** 1024-1026, (1976).

39. L. M. Sandratskii, M. Uhland J. Kübler, "Band theory for electronic and magnetic properties of α-Fe_2O_3," *J. Phys.: Condens. Matter.*, **8**, 983-989, (1996).

40. D. M. Sherman, "The electronic structure of Fe^{3+} coordination sites in iron oxides: Application to spectra, bond, and magnetism," *Phys. Chem. Minerals.*, **12**, 161-175, (1985).

41. K. F. McCarty, "Inelastic scattering in α-Fe_2O_3: phonon vs magnon scattering," *Solid State Communications*," **68**, 799-802, (1988).

42. S. H. Shim and T. S. Duffy, "Raman spectroscopy of Fe_2O_3 to 62 GPa," *American Mineralogist,* **87**, 318-326, (2001).

43. M.J. Massey, U. Baier, R. Merlin and W.H. Weber, "Effects of pressure and isotopic substitution on the Raman spectrum of α-Fe_2O_3: Identification of two-magnon scattering," *Phys. Rev. B: Condensed Matter*, **41,** 7822-7827, (1990).

44. T. P. Martin, R. Merlin, D.R. Huffman and M. Cardona, "Resonant two magnon Raman scattering in Fe_2O_3," *Solid State Commun.,* **22,** 565-567, (1977).

45. W. E. Vehse, K. H. Lee, S.I. Yun and W. A. Sibley, "Ni^{2+} emission in MgO, $KMgF_3$, $KZnF_3$ and MgF_2," *J. Lumin.*, **10**, 149-162, (1975).

46. M. V. Iversion and W. A. Sibley, "Temperature dependence of Ni^{2+} luminescence in $KZnF_3$, MgF_2 and MgO," *J. Lumin.*, **20**, 311-324, (1979).

47. J. H. W. deWit, A. F. Broersma and M. Stroband, "Surface instability and nonstoichiometry of α-Fe_2O_3," *J. Solid State Chem.*, **37**, 242-247, (1981).